CORE
Metadata, citation and similar papers at core.ac.uk
Provided by Hasanuddin University Repository

Design Optimization of a Floating Breakwater

by

Faisal MAHMUDDIN

A dissertation submitted in partial fulfillment for the degree of Doctor of Engineering

in the

Graduate School of Engineering

Department of Naval Architecture and Ocean Engineering

Division of Global Architecture

Osaka University

August 2012

"All humans are dead except those who have knowledge. And all those who have knowledge are asleep, except those who do good deeds."

Imam Ash-Shaafi'ee

OSAKA UNIVERSITY

Abstract

Graduate School of Engineering
Department of Naval Architecture and Ocean Engineering

Doctor of Engineering

by Faisal MAHMUDDIN

In order to design an optimal floating breakwater with a high performance in a wide range of frequencies, 2D and 3D analyses are performed in this study. The design starts with seeking an optimal 2D model shape. For this purpose, an optimization method called Genetic Algorithm (GA) combined with Boundary Element Method (BEM) is employed as the main calculation method. The accuracy of BEM analysis is confirmed using several relations such as Haskind-Newman and energy conservation relations. Moreover, since the investigated model will be an asymmetric shape, an experiment using a manufactured asymmetric model is also conducted to confirm that the present analysis could treat asymmetric body case correctly. From the experiment, a favorable agreement with numerical results can be found for both fixed and free motions cases which strengthen our confidence on the 2D analysis correctness.

However, because the optimal performance obtained in 2D analysis is expected to be different for some extent from real application, the performance of the corresponding model in 3D case is also analyzed. Higher order boundary element method (HOBEM) is employed for this purpose. 3D Wave effect and its effect to the floating breakwater performance are analyzed and discussed. For consideration of real model construction and installation, drift forces induced by waves are also computed. It is shown from this study that the combination of GA and BEM is effective in obtaining an optimal performance model. Moreover, by computing its the corresponding 3D model, it can also be shown that the 3D wave effect is small on motion amplitude while the wave elevation is found to be in 3D pattern even for a longer body length.

Acknowledgements

I am sincerely and heartily grateful to my supervisor, Professor Masashi Kashiwagi, for his continous excellent guidance, care and patience throughout the course. Despite his many other academic and professional commitments, he still could be able to provide me with an international top level atmosphere of research. His abundant support and invaluable assistance that he gave truly help the progression and smoothness of my doctoral program. It will be difficult to imagine having a better supervisor than him for my study.

My special thanks also to Professor Shigeru Naito for his constant caring and attention to my study. Even though, we did not have much time for discussion but his encouragement is much indeed appreciated.

Besides them, I am also truly indebted and thankful to Professor Munehiko Minoura and Dr. Guanghua He for their wise advice and insightful comments.

I also owe sincere and earnest thankfulness to Shimizu-san, for supporting me in the experiment. Helping to remove obstacles and resolve problems have been crucial for achieving the experiment objectives.

Furthermore, I would like to say that it is a great pleasure to spend time with all of my very nice and friendly lab mates. I highly appreciate the invitation to participate on sports activities and parties with halal food. Thanks for the friendship and memories.

I would like to thank my family members, especially my mothers and sisters for the pray and encouragement to pursue this degree.

Finally, I would like to thank everybody who was important to accomplish the dissertation, as well as expressing my apology that I could not mention personally one by one.

Osaka, August 2012

Faisal Mahmuddin

Contents

List of Figures

List of Tables

Abbreviations

2D	two **D**imensional
3D	three **D**imensional
B	**B**ottom **B**oundary **C**ondition
BEM	**B**oundary **E**lement **M**ethod
BIE	**B**oundary **I**ntegral **E**quation
F	**F**ree surface **B**oundary **C**ondition
GA	**G**enetic **A**lgorithm
H	body boundary condition
L	**L**aplace equation
PI	**P**erformance **I**ndex
HOBEM	**H**igher **O**rder **B**oundary **E**lement **Method**

Symbols

A	hydrodynamic added mass	kg
B	hydrodynamic damping coefficient	kgs^{-1}
b	half of body breadth	m
C	hydrodynamic restoring force	kgs^{-2}
C_R	reflection coefficient when body motions free	
C_T	transmission coefficient when body motions free	
d	body draught	m
E	diffraction hydrodynamic force	kgs^{-2}
F	radiation hydrodynamic force	kgs^{-2}
f_{ave}	average fitness	
f_{max}	maximum fitness	
G	center of gravity or Green function	
GM	metacenter height	m
g	gravitational acceleration	ms^{-2}
H	Kochin function	
I	moment of inertia	kgm^2
K	wave number in infinite depth water	m^{-1}
LWL	longest wavelength	m
M	total number of field points	
m	body mass or number of bits	
N	number of unknwon	
$\boldsymbol{n}$	normal vector	m
O	origin of coordinate system	

P	field point	
P_m	mutation probability	
P_c	crossover probability	
Q	source point	
OB	distance of center of buoyancy to buoyancy	m
OG	distance of center buoyancy to center of gravity	m
R	reflection coefficient when body motions are fixed	
T	transmission coefficient when body motions are fixed	
δ_{ij}	Kronecker's delta	
λ	wavelength	m
∇	gradient operator	m^{-1}
ω	angular frequency	rads^{-1}
$\Phi,\ \phi,\ \varphi$	velocity potential	$\mathrm{m}^2\mathrm{s}^{-1}$
ρ	water density	kgm^{-3}
ζ	wave elevation	m

Chapter 1

Introduction

1.1 Background

It is known that near-shore area has become an increasingly important area for people activities nowadays. It plays a significant role in supporting economic and social growth. As a result, it is necessary to protect this area from wave attack for people convenience. There are some choices of protection that can be installed ranging from simple structures such as rubble mound breakwater to more complex structures such as a caisson breakwater. Each type has its own advantages and disadvantages. These fixed-type structures are usually very efficient in protecting the shore but because of their high construction cost, they are usually installed only in shallow water area. The installation becomes more difficult and expensive as the water depth increases.

As a consequence, a free-floating-type breakwater becomes a more common choice in deep water sea. Besides its flexibility, fresh water circulation feasibility, etc., a floating-type breakwater is also cheaper and easier to be manufactured. Even though its performance is usually lower than fixed-type ones, the use of this type breakwater is becoming more popular.

However, even though the increase in practical demand of floating breakwater which attracts more attention of many researchers to perform research about floating breakwaters, the past research has shown that conventional-type floating breakwaters which usually have only a simple shape such as rectangular shape, could only attenuate waves in a limited range of frequency especially in short wavelength region. Example of such attempts can be found in Kashiwagi et al. [4] and Mahmuddin and Kashiwagi [5]. Consequently, it is needed to find a more efficient and optimal shape design even if it would make the model shape more complex.

For this purpose, a search optimization method called Genetic Algorithm (GA) combined with Boundary Elemement Method (BEM), are used to obtain an optimal model. It is known that GA has ability to find an optimal result based on defined fitness functions or criteria in a defined search space. Moreover, by choosing appropriate genetic operators, GA can avoid terminating at local optimum, which means the obtained result is the most optimal one globally. However, because GA is an undeterministic method, slightly different results might be obtained for different runs.

In this dissertation, the reflection and transmission coefficents, which are defined as the amount of incident wave which are reflected and transmitted, respectively, are used to determine the performance of a floating breakwater. Hence these parameters will be used as the fitness function. In order to obtain the reflection and transmission coefficients of a floating breakwater, Boundary Element Method (BEM) is employed. The BEM is based on the potential flow theory. It divides the body surface into a large number of panels in which the velocity potentials are to be determined. In 2D, the BEM is relatively an effective and fast numerical computation method with good enough accuracy. Consequently, it is very ideal and appropriate to combine it with GA which needs many iterations before an optimal result can be obtained.

After obtaining an optimal 2D model, the next step is to investigate the performance of this shape in 3D case. It is expected that the performance will decrease due to the so-called 3D wave effect. It is the effect due to the assumption that the length of 2D body is infinite which is not the case for 3D analysis. For the 3D analysis and computation, Higher Order Boundary Element Method (HOBEM) will be used.

In HOBEM, the body surface is also divided into a large number of panels. Each of these panels is represented by 9-node quadratic element. The velocity potentials at nodal points are then obtained by solving integral equations. It is also assumed that these velocity potentials are varied on these panels, so greater accuracy can be obtained with less number of panels compared to direct constant panel method. Using the velocity potentials and body motions, the wave elevation around the body can be obtained and compared to 2D results. For practical consideration, the analysis and computation of drift forces are also necessary. Moreover, a series of numerical accuracy confirmation using the energy conservation and Haskind-Newman relation is made to confirm the results.

1.2 Study Objectives and Organization

The main objective of this study is to obtain an optimal floating breakwater satisfying some criteria. In order to achieve this objective, the analysis will start with 2D case to simplify the problem. In 2D analysis, the optimization is performed by using genetic algorithm (GA) combined with boundary elemenet method (BEM). Even though accuracy of the computation is confirmed using several relations, it is necessary also to confirm it by an experiment. Consequently, a real model is manufactured and tested to check the real performance to be compared with computed ones. The analysis and discussion will be separated in 2 cases which are fixed and free-motion cases.

After confirming the accuracy of both GA and BEM, the next step will be analysing the performance of obtained model in 3D case. In this case, higher order boundary element method (HOBEM) is used. The same relations are used to confirm the accuracy of computations. The perfomance difference and 3D wave effect are presented and discussed. Moreover, drift forces are also computed for real installation consideration especially for body mooring.

In order to achieve the objective, the problem and solution procedure in this study needs to be arranged. The first chapter gives introduction and overview of the problem, motivation and objectives. In chapter 2, theoretical background of both GA and BEM are explained which is followed by presenting about the experiment used to compare and confirm the numerical results of BEM in chapter 3. In chapter 4, a comprehensive analysis and optimization results in 2D case will be explained, and then in chapter 5, the theoretical background of HOBEM analysis and computation results are described including discussion on its results. Finally, chapter 6 will summarize and conclude the results of the study.

Chapter 2

Theory of 2D Optimization Method

As the first step of design process, a model shape with an optimal performance should be obtained. For this purpose, Genetic Algorithm (GA) and Boundary Element Method (BEM) will be used as the main calculation methods. This chapter will explain the basic theory of these 2 main calculation methods.

2.1 Genetic Algorithm (GA)

2.1.1 Algorithm Principle

Genetic Algorithm is a general search and optimisation method based on the nature principle which is survival of the fittest or also known as natural selection. It is a part of evolutionary computing which has been widely studied and applied in many fields in engineering because many of the engineering problems involve finding optimal parameters, which might prove difficult for traditional methods but ideal for GA.

The main principle of GA is to mimic processes in the evolution theory. For a given specific problem to solve, a set of initial possible solutions inside a certain domain called search space, is randomly chosen. This set of solutions is called population which consists of certain number of individuals. Each individual is encoded in certain ways to construct a chromosome. A chromosome consists of certain number of genes. A gene represents a particular characteristic of an individual. The length and structures of a gene and chromosome depend on the type of encoding that is chosen.

By chance, some individuals are chosen to be mated or modified by genetic operators to obtain their offsprings. These offsprings are quantitatively evaluated using a metric called fitness function. GA will choose candidates for the next round based on the individual fitness using probabilistic function so that promising candidate will have higher probability to be chosen. Random changes are again introduced using genetic operators to obtain offsprings. These offspring then go on to the next generation, forming a new population to replace the old population. Consequently, those individuals which were worsened, or made no better, by the changes to their fitness will not be chosen by chance; but again, purely by chance, the random variations introduced into the population may have improved some individuals, making them into better, more complete or more efficient solutions to the problem.

The expectation is that the average fitness of the population will increase each round, and so by repeating this process for hundreds or thousands of rounds, very good solutions to the problem can be discovered. This process can be seen in Fig. 2.1.

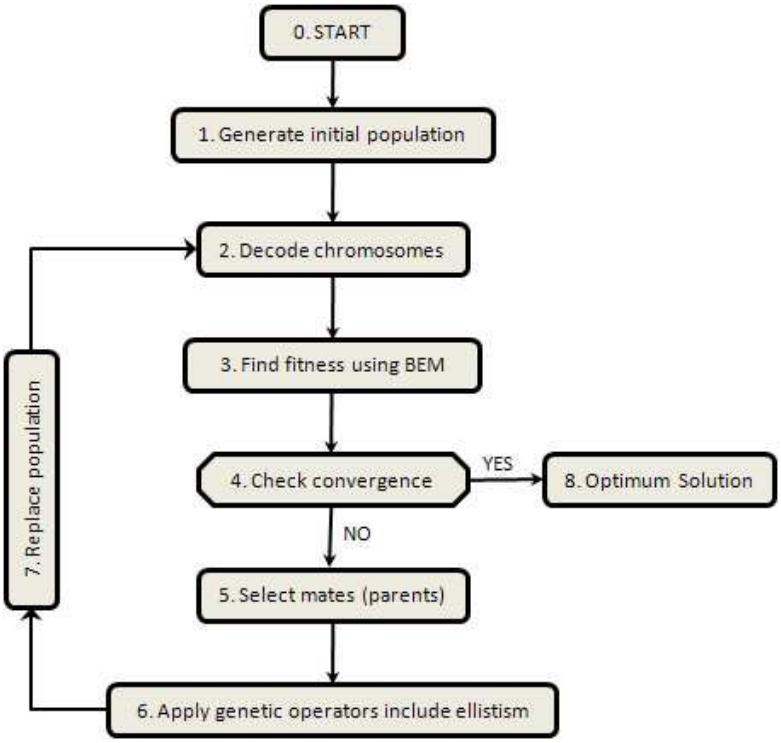

FIGURE 2.1: Workflow of GA

2.1.2 Encoding and Decoding

Before starting applying genetic operators to the chromosome of each individual, the representation of chromosome or genes of each individual needs to be encoded. There are some types of encoding such as binary encoding, value encoding, permutation encoding, and tree encoding. The type of encoding to be used depends on type of the problem to solve. In this study, binary encoding will be used. This encoding is the most common one to be used. In this encoding, each gene is represented by a string of 0s and 1s, where the digit at each position represents the value of some characteristics of the solution. The length of the string depends on the accuracy required. In general, we can say that if a variable is coded using m bits, the accuracy is approximately given as

$$\frac{x_U - x_L}{2^m} \tag{2.1}$$

where x_U and x_L are the highest and lowest values of the variable. An example of chromosomes with 4 genes where each gene is represented by 6 bits is shown in Fig. 2.2.

Chromosome 1	110111 100100 011101 010101
Chromosome 2	010011 001110 101001 101110

gene 1 gene 2 gene 3 gene 4

FIGURE 2.2: Example of chromosomes and genes

In this study, the gene string length will be 8 bits ($m = 8$) which means that each real number will be represented by 8 1s and/or 0s.

After encoding and modification by genetic operators, the chromosome will be decoded using the formula

$$(\text{decimal value})_i = \sum_{j=0}^{m_i-1} 2^j \alpha_j \tag{2.2}$$

where α_j denotes the bit values of $i-$th gene and m_i is the binary length of the gene. Decoding will transform binary numbers to real numbers which can be interpereted and computed by BEM.

2.1.3 Genetic Operators

Besides encoding, it is also necessary to define the genetic operators that will be implemented. The following genetic operators are applied in this study.

- Selection (reproduction) is the process of choosing parents for mating. The basic part of the selection process is to stochastically select from one population to create the basis of the next population by requiring that the fittest individuals have a greater chance of survival than weaker ones. There are

some methods of choosing individual to be parents such as roulette wheel selection, rank selection, steady state selection, etc. In this study, roulette wheel selection method is used. In this method, a random number is thrown and multipled by total fitness of all individuals in the population. The individual fitnesses are added together until the sum is greater than or equal to the product. The last individual to be added is the selected individual.

- Crossover is used to interchange limited parts of parents. The parents will be decided to undergo crossover or not based on crossover probability (P_c). Crossover method is separated into several types such as single point crossover, two points crossover, uniform crossover and arithmetic crossover. In this study, single point crossover will be used. In this crossover, only one point in the choromosome is selected for crossover. Binary string from beginning of chromosome to the crossover point is copied from one parent, the rest is copied from another parent.

- Mutation is used to flip the value of each bits of an individual. It is decided to apply mutation based on mutation probability (P_m). Mutation is used to introduce new characters into search space. It could guarantee the diversity of characteritics of population.

- Elitism is copying the fittest member of previous population if the maximum fitness of the new population is lower than this fittest member. It could guarantee the fittest individual is always copied to the next generation.

Besides some basic genetic operators above, there are still many more complex genetic operators which can be implemented if necessary. More detail about basic theory and application of GA can be found in for example Coley [6], Sivandam and Deepa [7], and Renner and Ekart [8].

2.1.4 Shape Parameterization

For easy remeshing and feasibility of a real model construction, the body surface is divided into two parts which are left and right parts as shown in Fig. 2.3. The bottom part will be just a straight line connecting these parts.

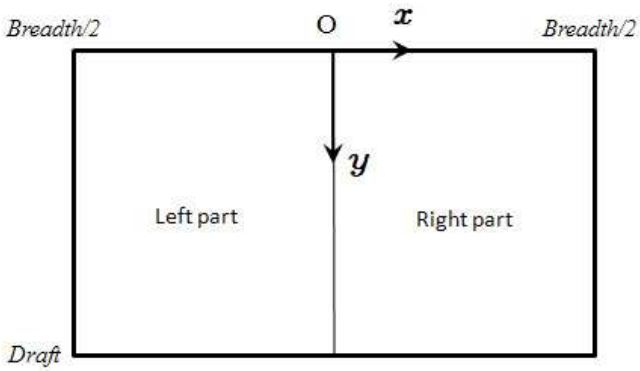

FIGURE 2.3: Body surface division

In each of divided body parts, the body surface will be represented by a Bezier curve which means that a complete body shape will consist of 2 Bezier curves and one straight line at the bottom. By using the Bezier curve, the boundary of body surface can be controlled easily using control points because the curvature of Bezier curve will never leave the bounding polygon formed by the control points. An example of shape representation using a Bezier curve for optimization is performed by Marco and Lanteri [9]. Fig. 2.4 shows an example of a bezier curve with 4 control points.

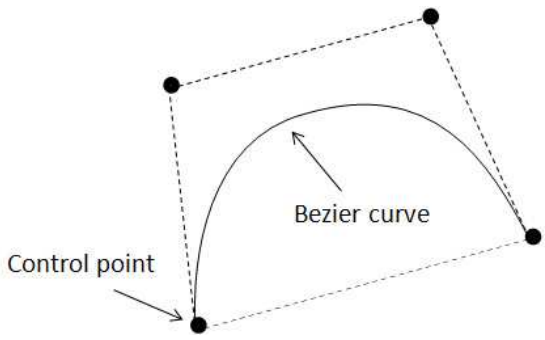

FIGURE 2.4: Bezier Curve

A Bezier curve of order n is defined by the Bernstein polynomials $B_{n,j}$ as follows:

$$B(t) = \sum_{i=0}^{n} B_{(n,i)} P_i \tag{2.3}$$

with

$$B_{(n,i)} = C_n^i t^i (1-t)^{(n-1)}, \quad C_n^i = \frac{n!}{i!(n-i)!} \tag{2.4}$$

where $t \in [0,1]$ and $P_i = (x_i, y_i)$ are the coordinates of the control points. The coordinates of the body surface can be defined as

$$x(t) = \sum_{i=0}^{n} C_n^i t^i (1-t)^{(n-i)} x_i \,, \tag{2.5}$$

$$y(t) = \sum_{i=0}^{n} C_n^i t^i (1-t)^{(n-i)} y_i \tag{2.6}$$

For each of left and right parts, a Bezier curve should be defined. On each part of the body, the values of $y_i \in [0,1]$ are fixed and the only parameters that vary are the ordinates x_i. Consequently, the chromosome is in the form

$$\text{chromosome } = (x_1, ..., x_8, x_9, ..., x_{16}) \tag{2.7}$$

Each gene in this chromosome acts as a control point to draw the body surface. In Eq. (2.7), the 8 first genes represent control points for the left side of the body surface and the 8 last genes represent the control points for the right side of the body surface. The drawn body surface is then discretized into a certain number of panels, with which hydrodynamic computations can be performed using BEM to obtain the fitness, known as perfomance index (PI) in the present study.

2.1.5 Fitness Function

In order to evaluate the performance of a floating breakwater and convergence of the calculation, the fitness measurement method needs to be defined. In the present study, there are 2 criteria which are used as fitness parameters which are Performance Index (PI) and Longest WaveLength (LWL). PI is defined as the area above the transmission-wave coefficient curve. As seen in Fig. 2.5, higher PI means low transmission, hence higher performance as a floating breakwater.

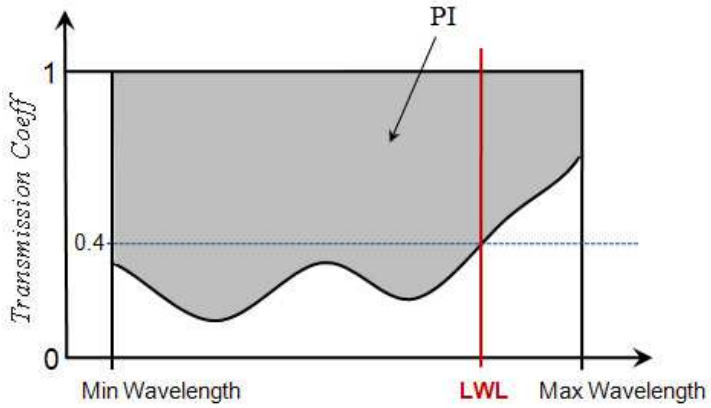

FIGURE 2.5: Definition of fitness

PI can be easily obtained by finding the area above the transmission coefficient curve using Simpson's integration method. Because the maximum nondimensional value of the transmission coefficient is equal to 1.0, then the maximum value of PI equals to Max wavelength - Min wavelength.

Another criterion or LWL is defined as the longest wavelength at which the body could transmit only 40% of incident wave at maximum. As also can be seen in Fig 2.5, LWL is also can be computed from wave transmission curve.

2.2 2D Boundary Element Method

This section will explain the Boundary Element Method (BEM) which is used to compute the reflection and transmission coefficients or the fitness function. The analysis will be in 2D case.

2.2.1 Boundary Conditions

In order to derive the boundary conditions, two coordinate systems are used which are the space-fixed coordinate system $(O - xy)$ and the body-fixed coordinate system $(\bar{O} - \bar{x}\bar{y})$ as shown in the Fig. 2.6

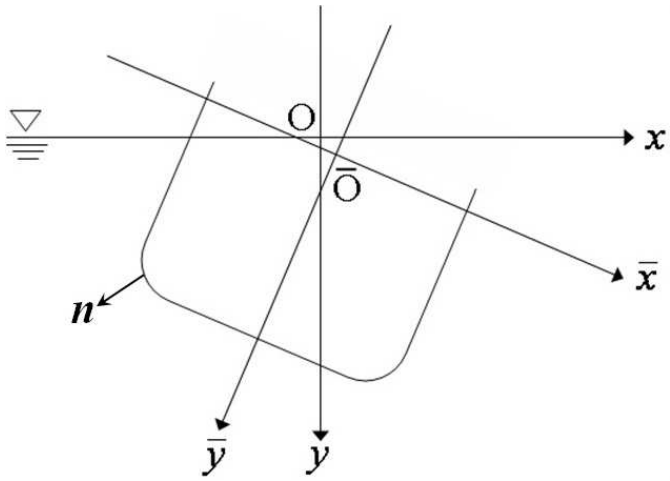

FIGURE 2.6: 2D coordinate systems

The body-motion amplitudes are assumed to be small. Their amplitudes around origin O expressed using complex amplitude notations can be written as

$$\left.\begin{aligned} \text{sway} \quad &: \mathrm{Re}[Xe^{i\omega t}] \equiv \mathrm{Re}[X_2 e^{i\omega t}] \\ \text{heave} \quad &: \mathrm{Re}[Ye^{i\omega t}] \equiv \mathrm{Re}[X_3 e^{i\omega t}] \\ \text{roll} \quad &: \mathrm{Re}[\Theta e^{i\omega t}] \equiv \mathrm{Re}[X_4 e^{i\omega t}] \end{aligned}\right\} \tag{2.8}$$

If we define the reference point $\boldsymbol{r} = (x, y)$ and $\bar{\boldsymbol{r}} = (\bar{x}, \bar{y})$, the relation between these points are

$$\left.\begin{aligned} \bar{\boldsymbol{r}} &= \boldsymbol{r} - \boldsymbol{\alpha} e^{i\omega t} \\ \boldsymbol{\alpha} &= \boldsymbol{i}(X_2 - X_4 y) + \boldsymbol{j}(X_3 + X_4 x) = \boldsymbol{i}X_2 + \boldsymbol{j}X_3 + \boldsymbol{k}X_4 \times \boldsymbol{r} \end{aligned}\right\} \tag{2.9}$$

By assuming the normal vector is positive facing outward the object, the body surface in the body-fixed coordinate system is

$$F(\bar{x}, \bar{y}) = \bar{y} - f(\bar{x}) = 0 \tag{2.10}$$

If we define Φ as a scalar satisfying the Laplace equation $\nabla^2 \Phi = 0$, which is known as the velocity potential, we can implement the kinematic boundary condition which states that the fluid and body-surface velocities in the direction normal to the body surface should be identical or in other words, the substantial derivative should be equal to zero. Using Eq. (2.10), we have

$$\begin{aligned} \frac{DF}{Dt} &= \left(\frac{\partial}{\partial t} + \nabla\Phi \cdot \nabla\right) F = 0 \\ &= \frac{\partial F}{\partial \bar{x}}\frac{\partial \bar{x}}{\partial t} + \frac{\partial F}{\partial \bar{y}}\frac{\partial \bar{y}}{\partial t} \\ &\quad + \nabla\Phi \left[\boldsymbol{i}\left(\frac{\partial F}{\partial \bar{x}}\frac{\partial \bar{x}}{\partial x} + \frac{\partial F}{\partial \bar{y}}\frac{\partial \bar{y}}{\partial x}\right) + \boldsymbol{j}\left(\frac{\partial F}{\partial \bar{x}}\frac{\partial \bar{x}}{\partial y} + \frac{\partial F}{\partial \bar{y}}\frac{\partial \bar{y}}{\partial y}\right)\right] = 0 \end{aligned} \tag{2.11}$$

Therefore

$$-i\omega\boldsymbol{\alpha}e^{i\omega t} \cdot \overline{\nabla} F + \nabla\phi e^{i\omega t}\left[\overline{\nabla} F - \boldsymbol{i}\frac{\partial \boldsymbol{\alpha}}{\partial x} e^{i\omega t}\overline{\nabla} F - \boldsymbol{j}\frac{\partial \boldsymbol{\alpha}}{\partial y} e^{i\omega t}\overline{\nabla} F\right] = 0 \tag{2.12}$$

where $\overline{\nabla}$ is the operator of derivative with respect to $(\bar{x}, \bar{y})$. Higher order terms due to distinction between the space-fixed and body-fixed coordinate systems can be eliminated in the linear theory so that $(\overline{x}, \overline{y})$ and (x, y) shall be considered the

same. As a result, Eq. (2.12) can now be shown as

$$\nabla\phi \cdot \nabla F = i\omega\boldsymbol{\alpha} \cdot \nabla F \tag{2.13}$$

We know the normal vector is defined by $\boldsymbol{n} = \dfrac{\nabla F}{|\nabla F|}$. Therefore, Eq. (2.13) will be

$$\nabla\phi \cdot \boldsymbol{n} = i\omega\boldsymbol{\alpha} \cdot \boldsymbol{n} = i\omega\left\{n_2(X_2 - X_4 y) + n_3(X_3 + X_4 x)\right\}, \tag{2.14}$$

which can be rewritten as

$$\frac{\partial\phi}{\partial n} = \sum_{j=2}^{4} i\omega X_j n_j \tag{2.15}$$

where

$$\left.\begin{array}{ll} n_2 = n_x = \dfrac{\partial x}{\partial n}, & n_3 = n_y = \dfrac{\partial y}{\partial n} \\ n_4 = n_3 x - n_2 y & (x_2 = x, x_3 = y) \end{array}\right\} \tag{2.16}$$

The body motions are caused by the incident wave, so in order to satisfy the boundary condition as in Eq. (2.15), the velocity potentials can be separated as

$$\phi = \phi_0 + \phi_2 + \phi_3 + \phi_4 + \phi_7 \equiv \frac{g\zeta_a}{i\omega}(\varphi_0 + \varphi_7) + \sum_{j=2}^{4} i\omega X_j \varphi_j, \tag{2.17}$$

where each component must satisfy the following body boundary conditions

$$\frac{\partial}{\partial n}(\varphi_0 + \varphi_7) = 0 \tag{2.18}$$

$$\frac{\partial}{\partial n}\varphi_j = n_j \quad (j = 2, 3, 4) \tag{2.19}$$

Here ϕ_0 is the incident wave potential and ϕ_7 is called the scattered wave potential, the sum of these $\phi_0 + \phi_7 = \phi_D$ is called the diffraction potential. Furthermore, ϕ_j is called the radiation potential which is caused by oscillating body in still fluid where j denotes the mode of motion ($j = 2$ is sway, $j = 3$ is heave, and $j = 4$ is

roll) as written in Eq. (2.8) and n_j ($j = 2 \sim 4$) denotes the j-th component of the normal vector as shown in Eq. (2.16).

2.2.2 Boundary Integral Equation and Green Function

Assuming an asymmetric body floating where the incident wave is coming from positive x-axis as shown in Fig. 2.7. The water depth is assumed to be infinite.

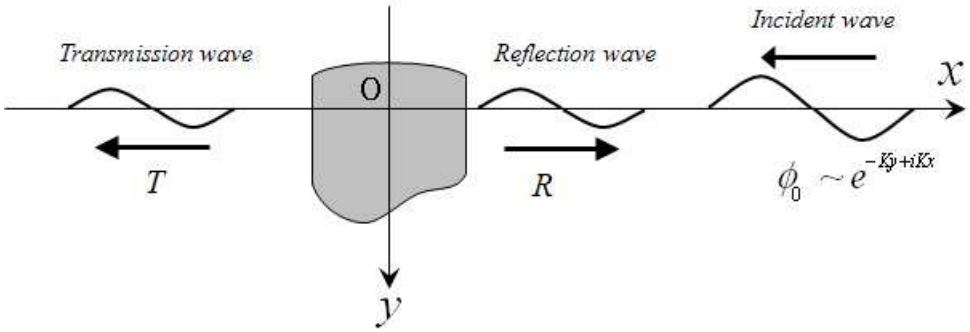

FIGURE 2.7: Coordinate system for an asymmetric floating body

There are some numerical solutions available for this kind of problem, but the present study will use boundary element method (BEM). The method will obtain the velocity potentials by solving the following boundary integral equation (BIE)

$$C(\mathrm{P})\phi_j(\mathrm{P}) + \int_{S_H} \phi_j(\mathrm{Q}) \frac{\partial}{\partial n_\mathrm{Q}} G(\mathrm{P};\mathrm{Q})\, ds(\mathrm{Q}) = \begin{cases} \displaystyle\int_{S_H} n_j(\mathrm{Q})\, G(\mathrm{P};\mathrm{Q})\, ds(\mathrm{Q}) & (j = 2 \sim 4) \\ \phi_0(\mathrm{P}) & (j = D) \end{cases} \tag{2.20}$$

where $\mathrm{P} = (x, y)$ and $\mathrm{Q} = (\xi, \eta)$ denote the field and integration points, respectively, located on the body surface S_H and $C(\mathrm{P})$ depends on the position of point P. It is equal to $1/2$ when P is on a smooth angle and 1 when P is in the fluid. Furthermore, $G(\mathrm{P};\mathrm{Q})$ represents the free-surface Green function in infinite water

depth. Its form is written as

$$\begin{aligned} G(\mathrm{P};\mathrm{Q}) &= \frac{1}{2\pi}\log\frac{r}{r_1} - \frac{1}{\pi}\lim_{\mu\to 0}\int_0^\infty \frac{e^{-ky}\cos kx}{k-(K-i\mu)}dk \\ &= \frac{1}{2\pi}\log\frac{r}{r_1} - \frac{1}{\pi}\mathrm{Re}\left[e^{-KZ}E_1(-KZ)\right] + ie^{-KZ} \end{aligned} \tag{2.21}$$

where

$$\left.\begin{matrix} r \\ r_1 \end{matrix}\right\} = \sqrt{(x-\xi)^2+(y\mp\eta)^2} \qquad Z = (y+\eta)+i|x-\xi| \tag{2.22}$$

and E_1 should be interpreted as an integral exponential function with complex variable. Derivation of Eq. (2.21) can be found in Wehausen and Laitone [10]. Here K is the wave number in infinite water depth of a progressive wave, satisfying the following dispersion relation

$$K = \frac{\omega^2}{g} \tag{2.23}$$

For a floating body as shown in Fig. 2.7, the velocity potential has the following form

$$\begin{aligned} \phi(x,y) &= \frac{g\zeta_a}{i\omega}\left\{\phi_D(x,y) - \sum_{i=2}^{4} KX_j\phi_j(x,y)\right\} \\ &\equiv \frac{g\zeta_a}{i\omega}\varphi(x,y) \end{aligned} \tag{2.24}$$

where ζ_a is the amplitude of incident wave and g is the acceleration of gravity. Because we consider the case of infinite water depth and incident waves is coming from positive x-axis, the incident wave potential takes the form

$$\phi_0 = \frac{g\zeta_a}{i\omega}e^{-Ky+iKx} \tag{2.25}$$

Substituting Eq. (2.21) into Eq. (2.20) with $C(\mathrm{P}) = 1$ for the solid angle, the asymptotic expression of the normalized velocity potential at $x \to \pm\infty$ can be obtained as follows

$$\begin{aligned}\varphi(x,y) &= \phi_D(x,y) - KX_j\phi_j(x,y) \\ &\sim e^{-Ky}\left[e^{iKx} + iH_4^{\pm}e^{\mp iKx} - iKX_jH_j^{\pm}e^{\mp iKx}\right]\end{aligned} \tag{2.26}$$

Here the upper or lower sign in the double sign is taken according to whether $x \to +\infty$ or $-\infty$, respectively. $H^{\pm}$ is the Kochin function which has general form as follow

$$H^{\pm}(K) = \int_{S_H}\left(\frac{\partial\phi}{\partial n} - \phi\frac{\partial}{\partial n}\right)e^{-K\eta\mp iK\xi}ds(\xi,\eta) \tag{2.27}$$

Separating the Kochin function into scattered ($H_7^{\pm}$) and radiated ($H_j^{\pm}$ ($j = 2 \sim 4$)) Kochin functions, their expressions can be defined explicitly as follows

$$H_7^{\pm}(K) = -\int_{S_H}\phi_D\frac{\partial}{\partial n}e^{-K\eta\pm iK\xi}ds \tag{2.28}$$

$$H_j^{\pm}(K) = \int_{S_H}\left(\frac{\partial\phi_j}{\partial n} - \phi_j\frac{\partial}{\partial n}\right)e^{-K\eta\pm iK\xi}ds \quad \text{for } j = 2 \sim 4 \tag{2.29}$$

From the dynamic boundary condition, the free surface wave elevation can be written as

$$\zeta = \frac{1}{g}\frac{\partial\Phi}{\partial t} + O(\Phi^2) \tag{2.30}$$

Rewriting (2.30) in terms of the Kochin function in (2.27) gives

$$\begin{aligned}\zeta(x,t) &\sim \mathrm{Re}[\zeta(x)e^{i\omega t}] \\ \zeta(x) &= \frac{i\omega}{g}\phi(x,0) = -\frac{\omega}{g}H^{\pm}(K)e^{\mp iKx} \quad \text{as } x \to \pm\infty\end{aligned} \tag{2.31}$$

The interaction between wave and body is actually a complex phenomenon. However, from linear-theory point of view, the real problem can be separated into the radiation and diffraction problems which implies that the Kochin function can also be separated into diffraction and radiation components. Substituting the velocity potential in Eq. (2.17) into the Kochin function in Eq. (2.27) gives

$$H^{\pm}(K) = \frac{g\zeta_a}{i\omega} H_7(K)^{\pm} + i\omega \sum_{j=2}^{4} X_j H_j^{\pm}(K) = \frac{g\zeta_a}{i\omega} \left\{ H_7^{\pm}(K) - K \sum_{j=2}^{4} \left(\frac{X_j}{\zeta_a} \right) H_j^{\pm}(K) \right\} \tag{2.32}$$

Substituting (2.32) into (2.31) to obtain the free surface elevation in terms of the Kochin function, we have

$$\begin{aligned} \zeta(x) &\sim -\frac{\omega}{g} \left\{ \frac{g\zeta_a}{i\omega} H_7^{\pm}(K) + i\omega \sum_{j=2}^{4} X_j H_j^{\pm}(K) \right\} e^{\mp iKx} \\ &= \{ i\zeta_a H_7^{\pm}(K) - iK \sum_{j=2}^{4} X_j H_j^{\pm}(K) \} e^{\mp iKx} \qquad as \;\; x \to \pm\infty \end{aligned} \tag{2.33}$$

which has a general form

$$\zeta(x,t) = \mathrm{Re}[\zeta(x) e^{i\omega t}] \equiv Re \left[\sum_{j=2}^{4} \zeta_j^{\pm} e^{i(\omega t \mp Kx)} + \zeta_7^{\pm} e^{i(\omega t \mp Kx)} \right] \tag{2.34}$$

where

$$\zeta_j^{\pm} = -iKX_j H_j^{\pm}(K) \qquad \text{radiation wave } (j = 2 \sim 4) \tag{2.35}$$

$$\zeta_7^{\pm} = i\zeta_a H_7^{\pm}(K) \qquad \text{scattered wave} \tag{2.36}$$

2.2.3 Hydrodynamics Forces

In order to determine the body motions, the hydrodynamic forces need to be computed. Because the force is a result of integration of the pressure, the pressure

equation taken from Bernoulli's equation is firstly linearized as

$$P(x,y,t) = -\rho\frac{\partial\phi}{\partial t} + \rho g y + O(\phi^2) \tag{2.37}$$

The pressure on an oscillating body in wave consists of 3 parts which are the hydrostatic, radiation, and diffraction parts. Those parts are expressed as follows :

$$\left.\begin{aligned} P(x,y,t) &= \mathrm{Re}\left[p(x,y)e^{i\omega t}\right] \\ p(x,y) &= p_s(x,y) + p_r(x,y) + p_d(x,y) \end{aligned}\right\} \tag{2.38}$$

where

$$p_s(x,y) = \rho g(X_3 + X_4 x) \tag{2.39}$$

$$p_r(x,y) = -\rho i\omega \sum_{j=2}^{4} i\omega X_j \varphi_j(x,y) \tag{2.40}$$

$$p_d(x,y) = -\rho i\omega \frac{g\zeta_a}{i\omega}(\varphi_0 + \varphi_7) = -\rho g a(\varphi_0 + \varphi_7) \tag{2.41}$$

In this case, the normal vector is defined to be positive when pointing into the fluid as stated before. For the radiation case, the hydrodynamic force due to the radiation part acting in the i-direction is computed by

$$F_i = -\int_{S_H} p_r(x,y) n_i ds = \rho(i\omega)^2 \sum_{j=2}^{4} X_j \int_{S_H} \varphi_j(x,y) n_i ds \equiv \sum_{j=2}^{4} f_{ij} \tag{2.42}$$

where

$$\begin{aligned} f_{ij} &= \rho(i\omega)^2 X_j \int_{S_H} \{\varphi_{jc} + i\varphi_{js}\} n_i ds \\ &= -(i\omega)^2 X_j \left[-\rho \int_{S_H} \varphi_{jc} n_i ds\right] - i\omega X_j \left[\rho\omega \int_{S_H} \varphi_{js} n_i ds\right] \end{aligned} \tag{2.43}$$

The term in the first braces is A_{ij} (added mass) and in the second braces is B_{ij} (damping force). Together with time dependent term $e^{i\omega t}$ for simplicity, added mass A_{ij} is proportional to the acceleration $(i\omega)^2 X_j e^{i\omega t}$ and the damping coefficient B_{ij} is proportional to the velocity $i\omega X_j e^{i\omega t}$. By extracting the body-motion amplitude X_j from these quantities, we can obtain the transfer function T_{ij} as follows

$$f_{ij} = T_{ij} X_j = -(i\omega)^2 \left\{ A_{ij} + \frac{1}{i\omega} B_{ij} \right\} X_j \tag{2.44}$$

where

$$T_{ij} = (i\omega)^2 \rho \int_{S_H} \varphi_j n_i ds = (i\omega)^2 \rho \int_{S_H} \varphi_j \frac{\partial \varphi_i}{\partial n} ds \tag{2.45}$$

For the diffraction case, the hydrodynamic force to be computed from Eq. (2.41) is given as follows

$$E_i = -\int_{S_H} p_d(x,y) n_i ds = \rho g \zeta_a \int_{S_H} \{\varphi_0(x,y) + \varphi_7(x,y)\} n_i ds \tag{2.46}$$

Eq. (2.46) is called the wave-exciting force, and particularly the force component related to the incident wave is called Froude-Krylov force. However, practical numerical computation is performed in nondimensional unit by using maximum half breadth $b = B/2$ as the characteristic length. Therefore, the added mass and damping coefficients from Eq. (2.43) and wave-excitating force from Eq. (2.46) should be nondimensionalized as follows

$$\left.\begin{aligned} A'_{ij} - iB'_{ij} &= \frac{A_{ij}}{\rho b^2 \epsilon_i \epsilon_j} - i \frac{B_{ij}}{\rho \omega b^2 \epsilon_i \epsilon_j} \\ E'_i &= \frac{E_i}{\rho g \zeta_a b \epsilon_i} \end{aligned}\right\} \tag{2.47}$$

For ϵ_j, when $j = 2$ and 3 then $\epsilon_j = 1$ and when $j = 4$ then $\epsilon_j = b$.

For the hydrostatic part, we can get the final formulae using line integral of Eq. (2.39) as before but for simplicity, Gauss' theorem will be used here. As we know

that the hydrostatic force acts only in the vertical direction which means that the contribution only exists in heave and roll. The general formula of the force is

$$S_i = -\int_{S_H} p_s n_i ds = -\rho g \int_{S_H} \{X_3 + xX_4\} n_i ds \tag{2.48}$$

The hydrodynamic force and moment must also be evaluated about the center of gravity G in considering the equations of body motion which will be described in the next subsection.

2.2.4 Equation of Motions

After computing the hydrodynamic forces, we need to solve the equations of motion of the floating body. In the subsection 2.2.1, we take the origin on the still water surface, but we need to make the center of gravity G as the reference point. In asymmetric body case as shown in Fig. 2.8 as an example, the position of center of gravity G will not be in the centerline.

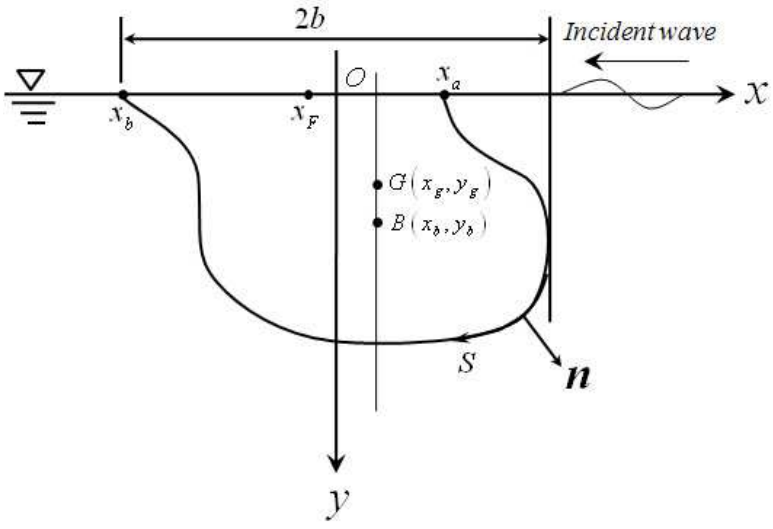

FIGURE 2.8: Coordinate system and notations of asymmetric body

Therefore, by denoting the distance of the center of gravity G in the positive y-axis (perpendicular downward) as y_g and in the positive x-axis as x_g, the relation of

motion amplitudes between these two origin points is shown as

$$X_2 = X_2^G + y_g X_4^G, \quad X_3 = X_3^G - x_g X_4^G, \quad X_4 = X_4^G \tag{2.49}$$

The body boundary condition in Eq. (2.19) and normal vectors about G are

$$\frac{\partial \phi_j^G}{\partial n} = n_j^G \qquad (j = 2 \sim 4) \tag{2.50}$$

$$\left.\begin{aligned} n_j^G &= n_j \text{ for } (j = 2, 3) \\ n_4^G &= n_4 - x_g n_y + y_g n_x \end{aligned}\right\} \tag{2.51}$$

Thus the velocity potentials about G can be written as follows

$$\left.\begin{aligned} \phi_j^G &= \phi_j \text{ for } (j = 2, 3) \\ \phi_4^G &= \phi_4 - x_g \phi_3 + y_g \phi_2 \end{aligned}\right\} \tag{2.52}$$

Using Eq. (2.51) and Eq. (2.52), we can write the hydrodynamic forces acting on the center of gravity using transform function T_{ij}, which is already defined in Eq. (2.45), as follows

- when i and j is 2 or 3

$$T_{ij}^G = T_{ij} \tag{2.53}$$

- when j is 4 and i is 2 or 3

$$T_{i4}^G = T_{i4} - x_g T_{i3} + y_g T_{i2} \tag{2.54}$$

- when i is 4 and j is 2 or 3

$$T_{4j}^G = T_{4j} - x_g T_{3j} + y_g T_{2j} \tag{2.55}$$

- when i and j are 4

$$T_{44}^G = T_{44} - x_g T_{43} + y_g T_{42} - x_g T_{34} + y_g T_{24} \tag{2.56}$$

Similarly, the conversion of the wave exciting force is as follows

- when i is 2 or 3

$$E_i^G = E_i \tag{2.57}$$

- when i is 4

$$E_4^G = E_4 - x_g E_3 + y_g E_2 \tag{2.58}$$

As stated before, the hydrostatic force and moment also need to be converted. The general formula in Eq. (2.48) can be converted to be

$$S_i^G = -\rho g \int_{S_H} \left\{ X_3^G + (x - x_g) X_4^G \right\} n_i^G ds \tag{2.59}$$

where in nondimensional form can be written as

$$S_i^G = -\rho g \zeta_a \epsilon_i \left[\frac{X_3^G}{\zeta_a} \int_{S_H} n_i^G ds + \frac{X_4^G b}{\zeta_a} \int_{S_H} (x - x_g) n_i^G ds \right] \tag{2.60}$$

The restoring force in heave can be obtained as

$$S_3^G = -\rho g \zeta_a b \left[\frac{X_3^G}{\zeta_a} \int_{S_H} n_3 ds + \frac{X_4^G b}{\zeta_a} \int_{S_H} (x - x_g) n_3 ds \right] \tag{2.61}$$

and in roll as

$$\begin{aligned} S_4^G = -\rho g \zeta_a b^2 \Bigg[& \frac{X_3^G}{\zeta_a} \int_{S_H} \{(x - x_g) n_y - (y - y_g) n_x\} ds \\ & + \frac{X_4^G b}{\zeta_a} \int_{S_H} (x - x_g) \{(x - x_g n_y - (y - y_g) n_x\} ds \Bigg] \end{aligned} \tag{2.62}$$

Using restoring force term C_{ij}, they can be shown as

$$S_i^G = -\rho g \zeta_a b \epsilon_i \left[\frac{X_3^G}{\zeta_a} C_{i3} + \frac{X_4^G b}{\zeta_a} C_{i4} \right] \tag{2.63}$$

where

$$C_{33} = \int_{S_H} n_3 ds = \int_{x_b}^{x_a} dx = x_a - x_b = B \tag{2.64}$$

$$\begin{aligned} C_{34} &= \int_{S_H} (x - x_g) n_3 ds = \int_{x_b}^{x_a} (x - x_g) dx \\ &= \frac{1}{2}(x_a^2 - x_b^2) - x_g(x_a - x_b) = B(x_F - x_g) \end{aligned} \tag{2.65}$$

$$\begin{aligned} C_{43} &= \int_{S_H} \{(x - x_g) n_y - (y - y_g) n_x\} ds \\ &= \int_{x_b}^{x_a} (x - x_g) dx = B(x_F - x_g) = C_{34} \end{aligned} \tag{2.66}$$

$$\begin{aligned} C_{44} &= \int_{S_H} (x - x_g) \{(x - x_g) n_y - (y - y_g) n_x\} ds \\ &= \int_{x_b}^{x_a} (x - x_g)^2 dx - \int\int (y - y_g) dx dy \\ &= \frac{1}{3}(x_a^3 - x_b^3) - x_g(x_a^2 - x_b^2) + x_g^2(x_a - x_b) - V y_B + V y_g \\ &= \nabla(y_g - y_B) + B\left(x_g^2 - 2 x_g x_F + \frac{1}{3}(x_a^2 + x_a x_b + x_b^2) \right) \end{aligned} \tag{2.67}$$

where B is the breadth of the body in the water plane, ∇ the displacement volume, x_a and x_b the horisontal distances from the origin in the water plane to positive and negative x-axes, respectively as shown in Fig. 2.8.

Summarizing the results above, we can write

$$\overline{F_i} = -\int_{S_H} (p_d + p_r + P_s) n_i^G ds \equiv \rho g \zeta_a b \epsilon_i F_i^G \tag{2.68}$$

where

$$F_i^G = E_i^G + Kb\sum_{j=2}^{4}\frac{X_j^G\epsilon_j}{\zeta_a}T_{ij}^G - \sum_{j=3}^{4}\frac{X_j^G\epsilon_j}{\zeta_a}C_{ij} \tag{2.69}$$

Using the hydrodynamic and the restoring forces above, we can establish the equation of motions as follows

$$-\omega^2\sum_{j=2}^{4}X_j^G m_{ij}\delta_{ij} = \overline{F_i} \qquad \text{for } (i=2\sim 4) \tag{2.70}$$

where δ_{ij} is the Kronecker's delta and the mass is

$$m_{jj} = \begin{cases} \rho\nabla & \text{for } (j=2,3) \\ \rho\nabla k^2 & \text{for } (j=4) \end{cases} \tag{2.71}$$

where k is the gyrational radius. Substituting Eq. (2.68) into Eq. (2.70), we can write

$$-\omega^2\sum_{j=2}^{4}X_j^G m_{ij}\delta_{ij} = \rho g\zeta_a b\epsilon_i F_i^G \tag{2.72}$$

$$-Kb\sum_{j=2}^{4}\frac{X_j^G\epsilon_j}{\zeta_a}\left(\frac{m_{ij}}{\rho b^2\epsilon_i\epsilon_j}\right)\delta_{ij} = F_i^G \tag{2.73}$$

or in another form as

$$\sum_{j=2}^{4}\frac{X_j^G\epsilon_j}{\zeta_a}\left\{-Kb\left(M_{ij}\delta_{ij}+T_{ij}^G\right)+C_{ij}\right\} = E_i^G \qquad (i=2\sim 4) \tag{2.74}$$

where the nondimensionalized mass M_{ij} is

$$M_{ij} = \frac{m_{ij}}{\rho b^2\epsilon_i\epsilon_j} \tag{2.75}$$

Other variables used in above equations are dimensionalized as follows

$$\left.\begin{aligned} &k' = \frac{k}{b}, \quad x'_g = \frac{x_g}{b}, \quad y'_g = \frac{y_g}{b}, \quad Z'_{ij} = A'_{ij} - iB'_{ij}, \\ &C'_{33} = \frac{C_{33}}{\rho g b} = \frac{B}{b}, \quad C'_{34} = \frac{C_{34}}{\rho g b^2}, \\ &C'_{43} = \frac{C_{43}}{\rho g b^2}, \quad C'_{44} = \frac{C_{44}}{\rho g b^3} = M\frac{\overline{GM}}{b} \end{aligned}\right\} \tag{2.76}$$

Using Eq. (2.49), the reference of the body motion amplitudes obtained by solving Eq. (2.74) are transformed to origin O and then will be used to compute the reflection and transmission coefficients as will be explained in the next subsection.

2.2.5 Reflection and Transmission Coefficient

Following the assumption of an asymmetric floating body with the incident wave coming from positive x-axis as shown in Fig. 2.7, the reflected wave will propagate with opposite direction to the incident wave ($x \to +\infty$), so from Eq. (2.33)

$$\zeta_R = i\zeta_a H_7^+(K) - iK\sum_{j=2}^{4} X_j H_j^+(K) \tag{2.77}$$

Using the incident wave amplitude to nondimensionalize Eq. (2.77), we obtain

$$C_R \equiv \frac{\zeta_R}{\zeta_a} = R - iK\sum_{j=2}^{4}\left(\frac{X_j}{\zeta_a}\right) H_j^+(K) \tag{2.78}$$

where

$$R = iH_7^+(K) \tag{2.79}$$

R is the reflection coefficient when the body is fixed and C_R is the corresponding cofficient when the body is free to oscillate. For transmitted wave, it will propagate

to $x \to -\infty$ and is given as the sum of wave caused by the incident wave and body oscillation as follows

$$\zeta_T = \zeta_a \left\{1 + iH_7^-(K)\right\} - iK \sum_{j=2}^{4} X_j H_j^-(K) \tag{2.80}$$

The nondimensional form can be written as

$$C_T \equiv \frac{\zeta_T}{\zeta_a} = T - iK \sum_{j=2}^{4} \left(\frac{X_j}{\zeta_a}\right) H_j^-(K) \tag{2.81}$$

where T is the transmitted coefficient when the body is fixed and C_T is when the body is free to oscillate in response to incoming incident wave. T is given as

$$T = 1 + iH_7^-(K) \tag{2.82}$$

2.2.6 Numerical Calculation of Velocity Potentials

In order to obtain the solution numerically, Eq. (2.20) is multiplied by 2π, so that with constant panel collocation method, we can write the following discretization formula

$$\pi\phi_j(\mathrm{P}_m) + \sum_{n=1}^{N} \phi_j(\mathrm{Q}_n) D_{mn} = \left\{ \begin{array}{ll} \displaystyle\sum_{n=1}^{N} n_j(\mathrm{Q}_n) S_{mn} & (j = 2 \sim 4) \\ 2\pi\phi_0(\mathrm{P}_m) & (j = D) \end{array} \right\} \tag{2.83}$$

where $m = 1 \sim N$ and the matrix coefficients are

$$D_{mn} = \int_{S_H} \frac{\partial}{\partial n_Q} \left\{ \log \frac{r}{r_1} - 2F_C(x - \xi, y + \eta) \right\} ds(\xi, \eta) \tag{2.84}$$

$$S_{mn} = \int_{S_H} \left\{ \log \frac{r}{r_1} - 2F_C(x - \xi, y + \eta) \right\} ds(\xi, \eta) \tag{2.85}$$

where $F_C(x-\xi, y+\eta)$ is the regular part of the Green function. This regular part has the following form

$$F_C(x-\xi, y+\eta) = \mathrm{Re}\int_0^\infty \frac{e^{-k(y+\eta)-ik|x-\xi|}}{k-K}dk - \pi i e^{-K(y+\eta)}\cos K(x-\xi) \quad (2.86)$$

Solving Eq. (2.86) will lead us to the following equation

$$F_C(x-\xi, y+\eta) = \mathrm{Re}\left[e^{-Z}E_1(-Z)\right] - \pi i e^{-Z} \quad (2.87)$$

where E_1 has the same definition as used in Eq. (2.21). Derivation and more detail about Eq. (2.87) can be found in Kashiwagi et al. [11].

In order to get rid of the irregular frequencies when solving Eq. (2.83), the method developed by Haraguchi and Ohmatsu [12] will be used. By considering the field point on the free surface inside the body, the first term of left side $\pi\phi_j(\mathrm{P}_m)$ which will vanish. At this time, if the right side of Eq. (2.83) is symbolically expressed as R_{jm}, and if we express $\phi_j(\mathrm{Q}_n) \equiv \phi_j^n$, then it will yield the simultaneous equations as follows:

$$\sum_{n=1}^{N} D_{mn}\phi_j^n = R_{jm} \quad (m = 1 \sim N, N+1, \ldots M) \quad (2.88)$$

where

$$D_{mn} = \begin{cases} \pi\delta_{mn} + D_{mn} & (m = 1 \sim N) \\ D_{mn} & (m = N+1 \sim M) \end{cases} \quad (2.89)$$

On the free surface inside the floating body, field points P_m are taken as number $m = N+1, \ldots M$. Because the number of equations M is larger than the number of unknown N, this simultaneous equations will be solved using the least-square method. For that purpose, we write the least-square method as

$$E = \sum_{m=1}^{M}\left[\sum_{n=1}^{N} D_{mn}\phi_j^n - R_{jm}\right]^2 \quad (2.90)$$

The condition for minimizing the error E defined above is $\partial E/\partial \phi_j^k = 0$ $(k = 1, 2, ...N)$, thus we can obtain

$$\sum_{n=1}^{N} \left\{ \sum_{m=1}^{M} D_{mn} D_{mk} \right\} \phi_j^n = \sum_{m=1}^{M} R_{jm} D_{mk} \quad \text{for } k = 1 \sim N \tag{2.91}$$

Now, there are N numbers of unknowns and N dimension of simultaneous equations. We can solve these equations using the general method such as the Gauss elimination method so that we can obtain the final velocity potentials on the body surface of floating body. Once the velocity potentials on the body surface are determined, it is straightforward to compute the hydrodynamic forces using Eqs. (2.43) and (2.46).

Chapter 3

Model Experiment

3.1 Introduction

In order to confirm correctness and accuracy of present analysis and numerical results, an experiment is conducted at the 2D wave channel at Department of Naval Architecture & Ocean Engineering, Osaka University. The tested model used in experiment is an an asymmetric body which has a shape shown in Fig. 3.1 together with notations used in the analysis.

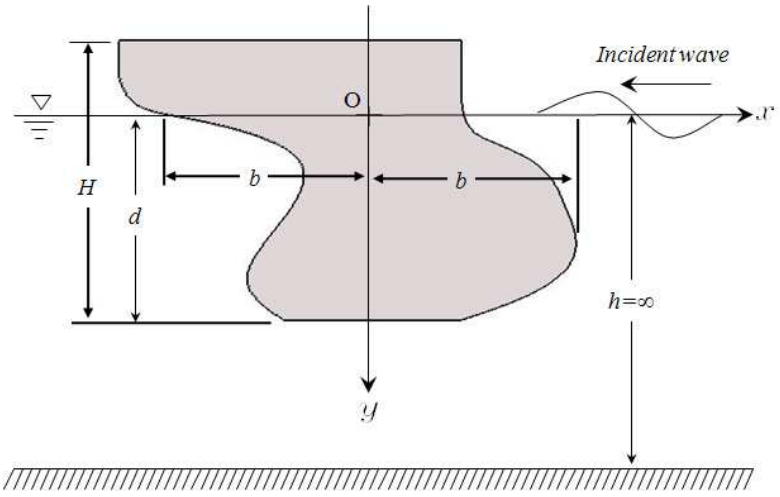

FIGURE 3.1: Shape, notations and coordinate system of tested model

Since the experiment aims to validate the numerical analysis for general body shapes especially for an asymmetric one, the shape of tested body was determined as shown in Fig. 3.1. This shape represents an asymmetric case because the submerged area in the right side is significantly larger than that in the left side, which means the horizontal shift in the center of buoyancy is also significant. As a result, the asymmetric effects could be realized with this shape.

The dimensions of the model based on the notations in Fig. 3.1 are shown in Table 3.1 including some of its geometrical parameters. Half of maximum breath (b) is used as the representative length for nondimensionalization. The dimensions of the model for manufacturing were determined by considering the dimensions of the wave channel.

TABLE 3.1: Tested model dimensions

Parameters	Dimensional (m)	Nondimensional
Height (H)	0.34	1.36
Half of max breadth (b)	0.25	1.0
Draft (d)	0.25	1.0
Length (L)	0.297	1.188
Center of gravity (OG)	0.1166	0.4664
Roll of gyrational radius (KZZ)	0.1365	0.546
Center of buoyancy-x (OBx)	0.0415	0.166
Center of buoyancy-y (OBy)	0.128	0.512

3.2 Manufactured Model

The tested model is ordered and manufactured at a specific company to guarantee its geometrical precision and wood is used as the material to acquire enough strength. Photos of the model after manufacturing are shown in Fig. 3.2.

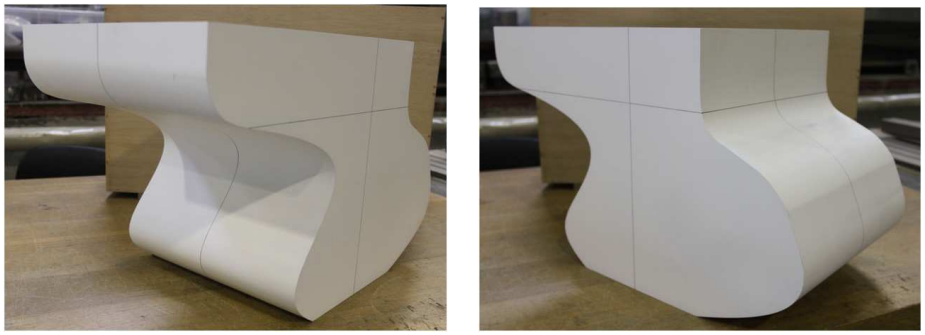

(a) (b)

FIGURE 3.2: Manufactured model used in the experiment

In order to align the waterline with water surface at the water channel, some weights are placed and adjusted inside the model. However, because of these weights adjustment, the geometrical parameters which are needed in numerical computation such as roll gyrational radius (KZZ) and metacentric height (GM) will obviously change. As shown in Fig. 3.1, the space for weights is very limited so it is quite difficult to freely adjust the weight to obtain desired KZZ and GM. As a consequent, the results obtained from this experiment may not represent the maximum performance of the model.

3.3 Experiment Preparation

Before conducting the experiment, the geometrical data of the model needs to be known as input in numerical computation. These data are the roll gyrational radius (KZZ) and metacentric height (GM). In order to obtain these data, an oscillation table as shown in Fig. 3.3 is used to obtain the center of gravity (OG) and the moment of inertia (I) of the model.

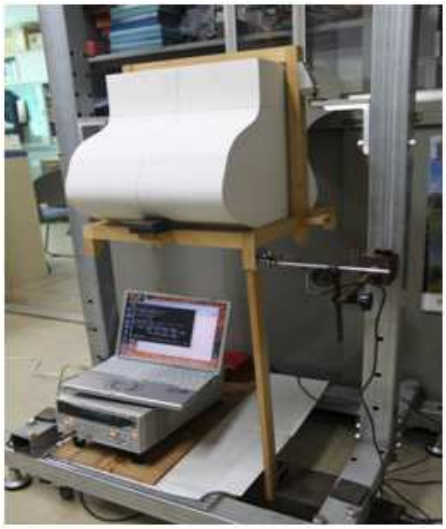

FIGURE 3.3: Oscillation table

The value of KZZ and GM can be determined easily after obtaining OG and I. The obtained data which are also used in numerical computation, are shown in Table 3.1.

3.4 2D Water Channel

The wave channel at Osaka University is shown in Fig. 3.4(a). This wave channel is equipped with piston type wave maker as shown in Fig. 3.4(b). The particular dimension of the channel are shown in Table 3.2.

TABLE 3.2: Particular Dimension of Wave Channel

Parameters	Value (m)
Length	14.00
Breadth	0.35
Height	0.70

The water depth used in the experiment is 0.53 m which would be appropriate to satisfy the infinite water assumption used in the numerical analysis.

(a) (b)

FIGURE 3.4: Wave channel

3.5 Experiment Setup

The main objective of the experiment is to measure the body motions and transmitted wave amplitude. For measuring the wave amplitude, three capacitance-type wave probes are used, while potentiometers installed inside the model to measure the heave and roll motions. The sway motion is measured using laser-type distance probe placed on the guide rail of wave channel near the body. The position of the wave probes and other settings of the experiment are shown in Fig. 3.5.

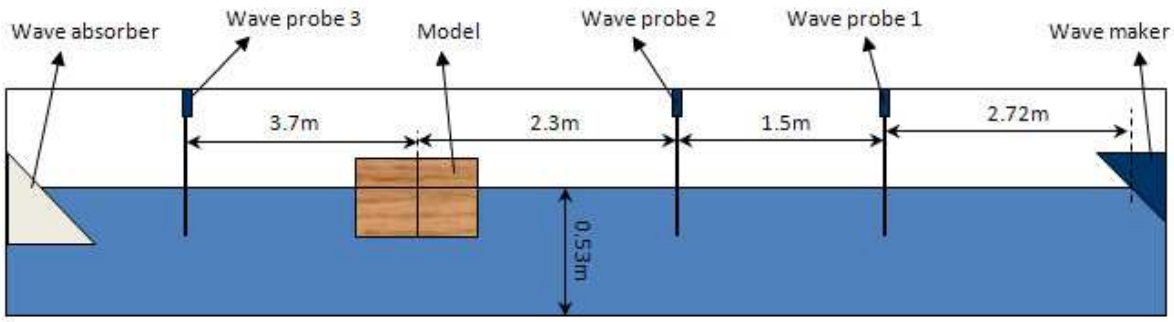

FIGURE 3.5: Experiment setting

Following the assumption used in the mathematical formulation, the incident wave is set to be coming from positive x-axis. The experiment is divided into two cases which are :

(1) the diffraction case : the body is fixed, no body motions are allowed.

(2) the motion-free case : the body oscillates freely in sway, heave and roll motions.

In this experiment, the important data that need to be measured are the transmitted wave amplitude and body motions. The transmitted wave is measured at wave probe 3 in Fig. 3.5 and body motion amplitudes are measured at the center of the body. These data are nondimensionalized using incident-wave amplitude measured at wave probe 1. The incident waves are measured at the beginning of incoming waves before this wave is mixed with reflected wave coming back from the body.

3.6 Results and Analysis

The obtained data are collected and analyzed. The obtained geometrical data are used to produce the results of numerical analysis which will be used to compare with the experimental ones. Following the numerical analysis, the experiment is also conducted for two cases which are fixed-motion and free-motion cases.

a. Fixed-Motion Case

   The results of the fixed-motion case are shown in Fig. 3.6 for the amplitude of transmission wave. In this figure, an acceptable agreement can be observed between measured and numerical results. Slight discrepancy may be attributed to geometrical nonlinearity near the free surface. This result can be considered as a preliminary validation of the analysis.

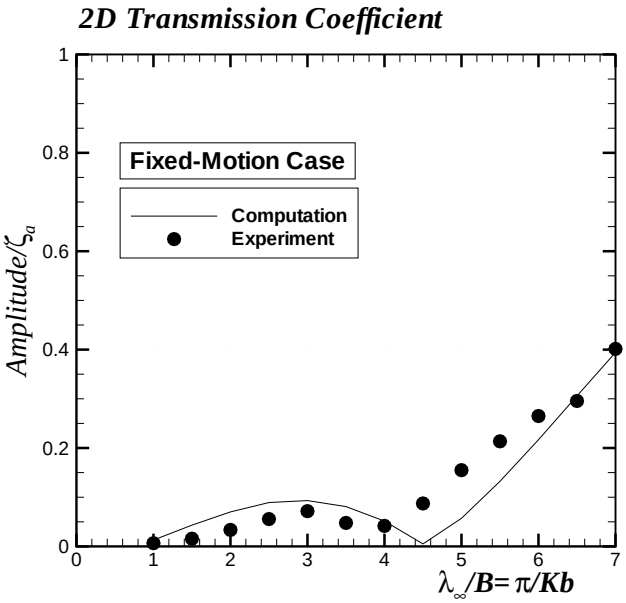

FIGURE 3.6: Transmission coefficent in fixed-motion case

b. Free-Motion Case

For the second case, which is more important in this study, the body motions are set free in sway, heave, and roll. The results of body motions are shown in Fig. 3.7(a), (b), and (c) for sway, heave, and roll motions, respectively. In these figures, the phase of each motion is also shown.

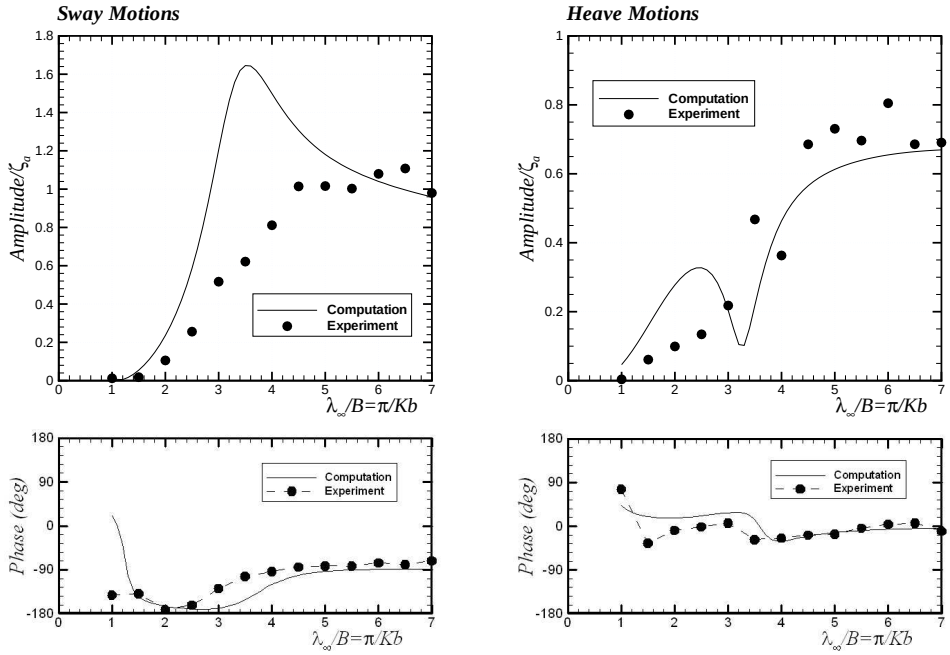

(a) (b)

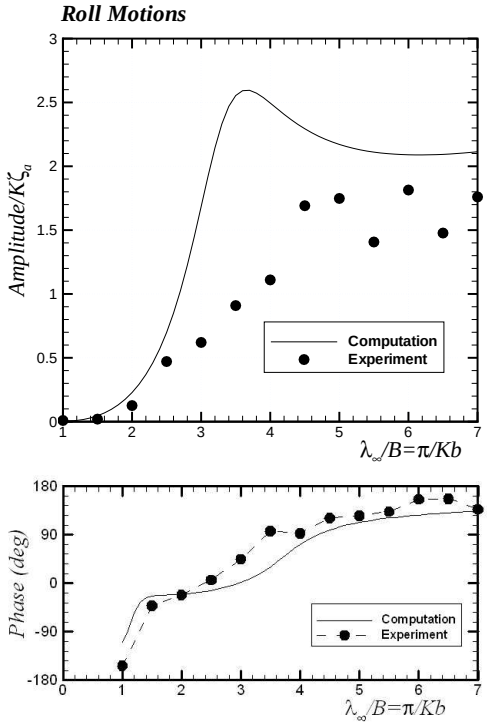

(c)

FIGURE 3.7: Motions amplitude and phase

In Fig. 3.7, it can be seen that the numerical results overpredict measured values especially near the peak of roll amplitude which corresponds to the natural frequency in roll. This discrepancy may be attributed to the effect of viscous damping. Since the present study is based on the potential flow theory, the viscous damping is not considered. Since the present model is asymmetric, all modes of body motion are coupled. Thus we can see rapid variation near the roll natural frequency even in sway and heave, which can be observed in measured results especially in the phase of heave. From these results, we can say that the agreement of the numerical results with measured ones for body motions is also relatively good.

The results for transmitted waves are shown in the following Fig. 3.8

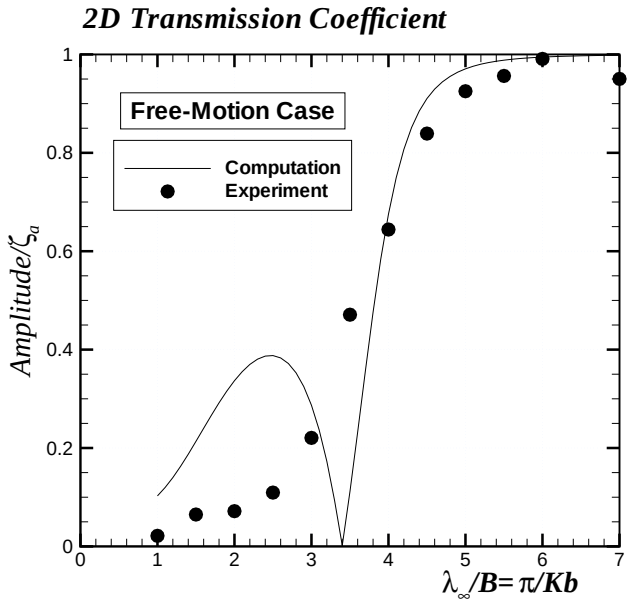

FIGURE 3.8: Transmission coefficent in free-motion case

From Fig. 3.8, even though some discrepancies can be found especially in short wavelength region, the overall trend seems to be acceptable. As a result, we can conclude that the analysis method is reasonable and can be incorporated in the GA optimization to compute the fitness function.

Chapter 4

Optimization Results Analysis

4.1 Parameters and Constraints

As a preliminary stage of GA optimization process, it is needed to determine some parameters such as mutation probability (P_m) and crossover probability (P_c). In order to understand the effect of these parameters and confirm correctness of the results, computations are performed by varying these values.

Following the dimension of tested body, the draft/breadth ratio is set equal to 1.0. Other parameters used in this computation are shown in Table 4.1. It is also important to note that the vertical position of the center of gravity (OG) and the roll gyrational radius (KZZ) are assumed and set to be constant in the entire computation which are also shown in Table 4.1 as nondimensional values in terms of half breadth (b). These values can be measured and adjusted later if necessary. It is important to keep in mind that because GA is an undeterministic process, there is always a possibility to find slightly different solutions for the same problem with different run.

TABLE 4.1: Parameters used in GA

Parameters	Value
No. of population	30
Selection scheme	Roulette wheel
Crossover scheme	Single point
Other operator	Ellitism
Minimum wavelength	0.2
Maximum wavelength	7.0
Maximum PI	6.8
Draft/Half breath ratio	1.0
$OG/(B/2)$	0.8
$K_{ZZ}/(B/2)$	0.6

An example of computed results is shown in Fig. 4.1 for the maximum fitness (f_{max}) and average fitness (f_{ave}) of a GA computation when P_m =0 and P_c =0.5. In this computation, the fitness function considered is only performance index (PI).

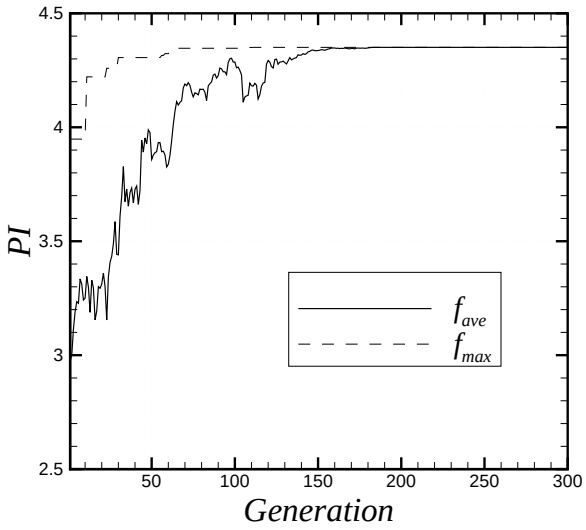

FIGURE 4.1: The average and maximum values of fitness (PI) in GA computation with P_m=0 and P_c=0.5

From Fig. 4.1, we can observe that without mutation, the average fitness will increase until the maximum fitness. This implies that in the GA computation, high performance models will appear while poor performance models will decay. This conclusion is consistent with the fundamental principle of GA which is survival of the fittest. Furthermore, in order to know the effect of P_c, GA computations were performed for different P_c with P_m=0.5 fixed. The computation results are shown in Fig. 4.2.

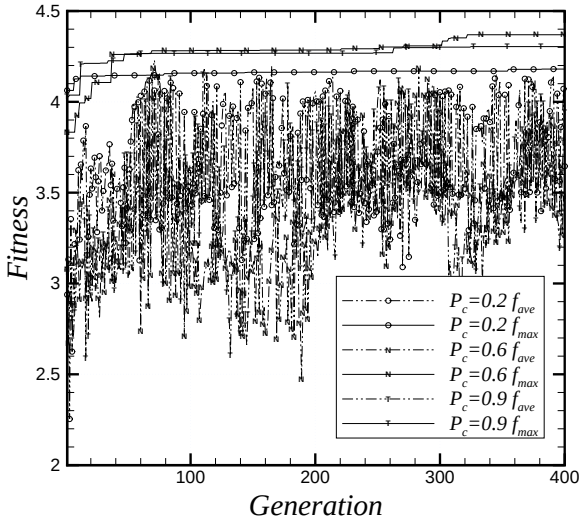

FIGURE 4.2: The average and maximum values of fitness (PI) in GA computation for P_m=0.5 and various values of P_c

From Fig. 4.2, we can see that setting higher P_c does not necessarily mean that a high performance model can be obtained. This is because higher P_c would also mean higher probability of losing some of the best individuals from previous generation.

Another important thing to note from this figure is that f_{ave} will not increase because the mutation is included in the computation. When the mutation is included, the computation will mutate some individuals which could also include mutating some good performance individuals to introduce new information or new identities so that genetic diversity can be maintained in the population. Preserving

the diversity can avoid the computation to terminate at a local optimum performance. However, using a very large P_m can have disastrous effect on computed results because mutating a large number of good performance models could make the convergence slow. So the reasonable values of P_c and P_m will depend on the encountered problem.

4.2 Results and Analysis

From the computation results in Figs. 4.1 and 4.2, we can see the consistency of the results with the fundamental theory of GA. Consequently, we can say that GA has been successfully implemented for the model shape optimization combined with BEM. By considering preliminary results, a computation is performed with P_c=0.6 and P_m=0.5. The number of population in each generation is also increased to be 40 for a faster convergence. All other data used are the same as shown in Table 4.1. Moreover, another criterion defined in Chapter 2 which is LWL, is also imposed in this computation.

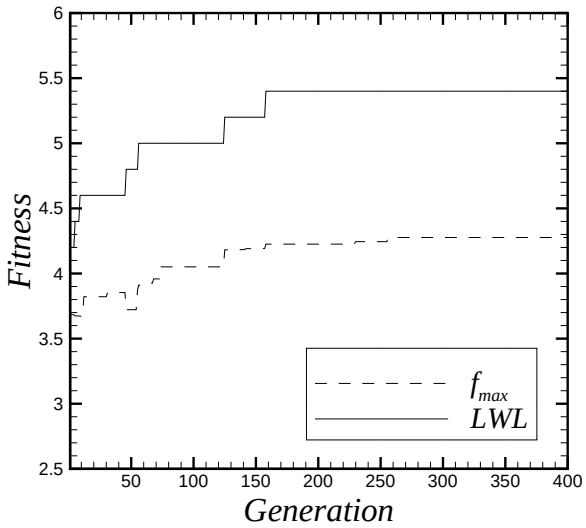

FIGURE 4.3: f_{max} and LWL of simulation with additional criteria

Computed results with these criteria are shown in Fig. 4.3. The computation is judged to be converged when there is no further fitness improvement for more than 100 generations. In Fig. 4.3, we can notice that even though the operator elitism is used, the value of f_{max} reduces at certain points. This is because the criterion of transmitting maximum 40% of incident wave at LWL is superior to having higher performance index (PI). Besides that, we can also see that the final f_{max} is slightly lower than that in the previous computation shown in Fig. 4.2 which is a consequence of implementation of the additional criteria. In order to see the process of GA to obtain the optimal model, the fittest model and its performance in some particular generations obtained in Fig. 4.3 are shown in Fig. 4.4 below.

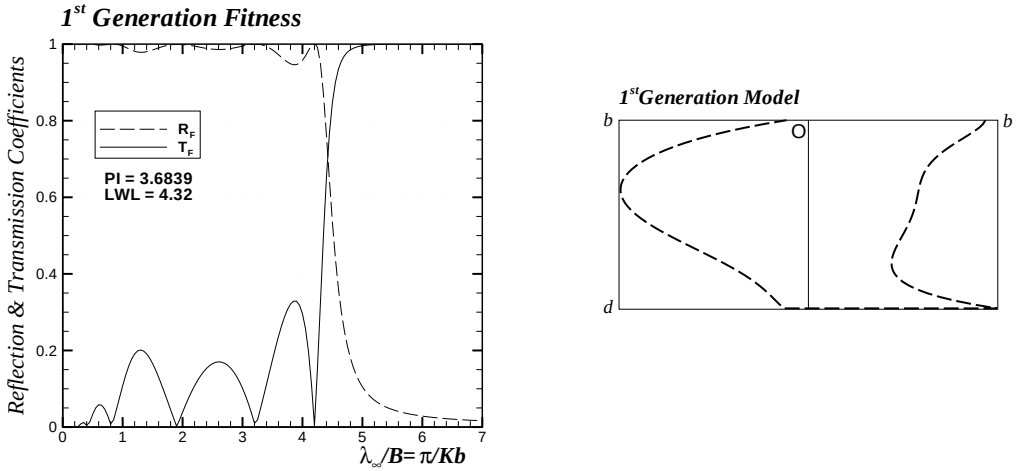

(a) Optimal model in 1st Generation

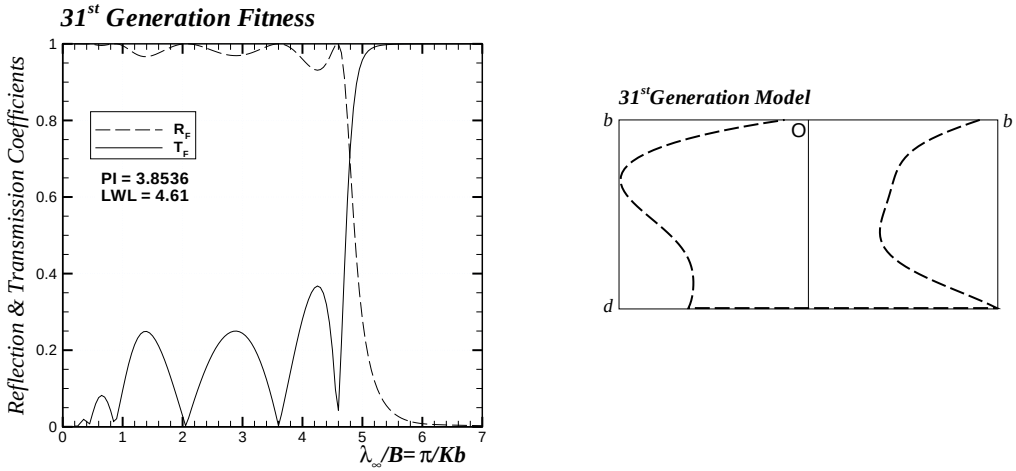

(b) Optimal model in 31st Generation

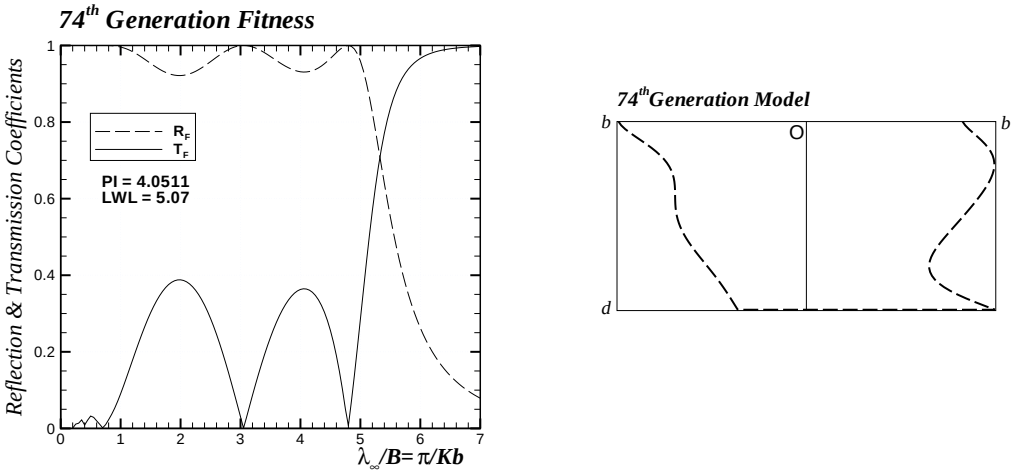

(c) Optimal model in 74$^{\text{th}}$ Generation

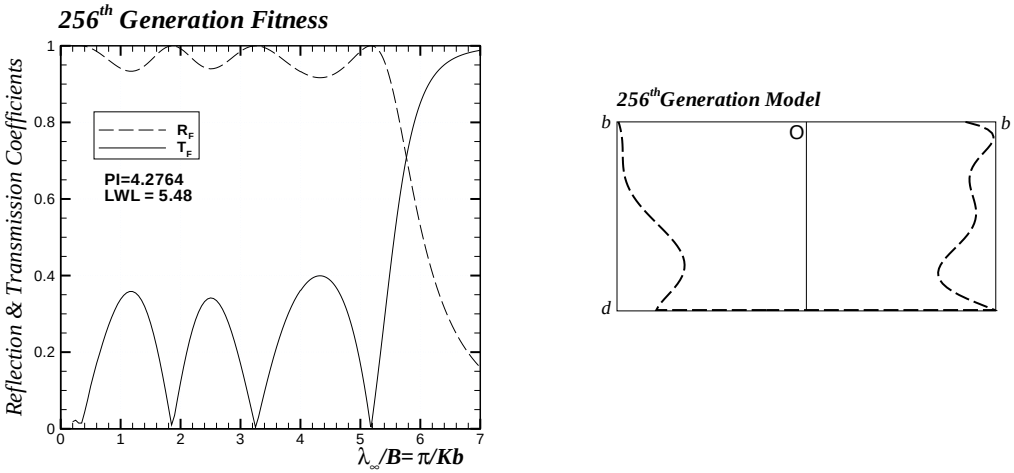

(d) Optimal model in 256$^{\text{th}}$ Generation

FIGURE 4.4: Fittest model and its performance in some particular generations

The generations shown in Fig. 4.4 are the ones where the performance improvements are obtained based on the result in Fig. 4.3. We can see from Fig. 4.4 that as the number of computations increases, obtained LWL will also increase, which shows the ability of GA to find other best shapes satisfying defined criteria when the computation is continued for next generations until the computation converges.

As shown in Fig. 4.4(d), the optimal model is obtained in the 256$^{\text{th}}$ generation. However, at the bottom part of the obtained body, a sharp edge in left and right sides can be seen. Considering the practical and construction requirements, this

edge should be modified to be blunt. The shape of the model after modification is shown in Fig. 4.5.

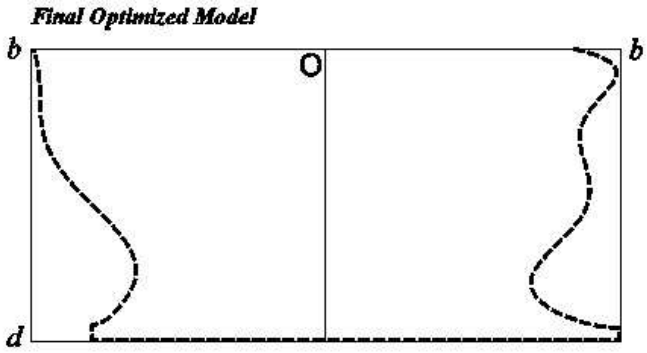

FIGURE 4.5: Modified final shape for the model

Since the modification of the body shape may affect the performance, it is needed to adjust the resonant frequency of the model to keep the performance satisfying the defined criteria by adjusting the center of gravity (OG) and the roll gyrational radius (KZZ). For this purpose, OG is set equal to 0.82 and KZZ is set equal to 0.614 in nondimensional value.

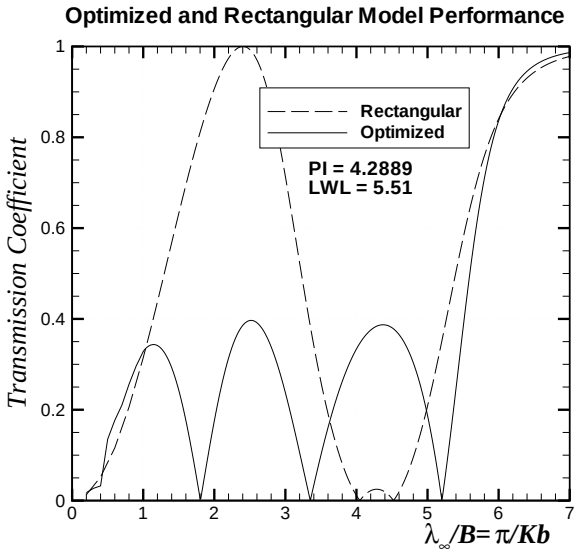

FIGURE 4.6: Transmission coefficients of the modified final model and corresponding rectangular shape

A comparison of the performance between the modified final and rectangular models can be seen in Fig. 4.6, from which an obvious improvement of the performance can be seen except in a very long wavelength region. In this region, it needs a larger draft over breadth ratio (deeper body dimension) to attenuate the transmitted wave. The geometrical data used to compute for the rectangular shape are the same as those used for the modified final shape.

Furthermore, it can also be noted from Fig. 4.6 that the performance of modified final model in terms of PI and LWL slightly increases compared to the original one. Moreover, high performance model could be obtained by adjusting nicely the position of waveless frequencies (where the transmission wave becomes zero) to maximize the results. For comparison to 3D computation results, the reflection and transmission coefficients for fixed-motions case are shown in Fig. 4.7 and its motion amplitudes are shown in Fig. 4.8

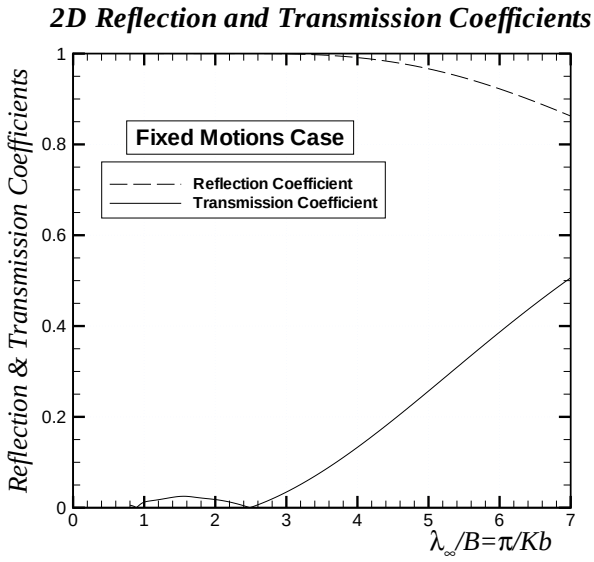

FIGURE 4.7: Reflection and transmission coefficients of optimized model for fixed-motion case

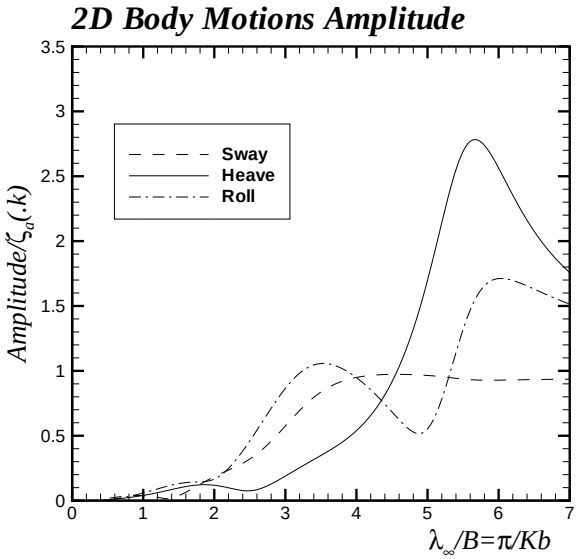

FIGURE 4.8: Body motion amplitudes of optimized 2D model

Chapter 5

3D Performance Analysis

In order to investigate the actual performance of an optimized 2D floating breakwater model which is previously obtained by genetic algorithm (GA) in the previous section, the performance and characteristics in terms of reflection and transmission coefficients of the corresponding 3D model of this shape are computed and analyzed. Different assumption used in formulation of 2D and 3D analysis will obviously lead to different computation results. However, by extending the length of model in 3D analysis, the similar trend of performance to 2D analysis can be obtained and the effect of the so-called 3D wave effect can be realized in both of fixed and free-motion cases. For consideration of real construction of the model, the drift force of the model is also computed. Higher order boundary element method (HOBEM), which is based on the potential flow theory and uses quadrilateral panels, is used as the main computation method. The accuracy of the computation is confirmed by a series of numerical check using several relations such as Haskind-Newman and energy relations.

5.1 Solution Method

5.1.1 Mathematical Formulations

The present study is concerned with the development of floating breakwaters of arbitrary shape with high performance in the wave reflection. However, considering realistic situations, the body shapes are assumed to be symmetric in the longitudinal direction but can be asymmetric in general in the transverse direction. The coordinate system adopted is shown in Fig. 5.1, where the body shape in the plane can be arbitrary but is assumed symmetric with respect to the x-axis.

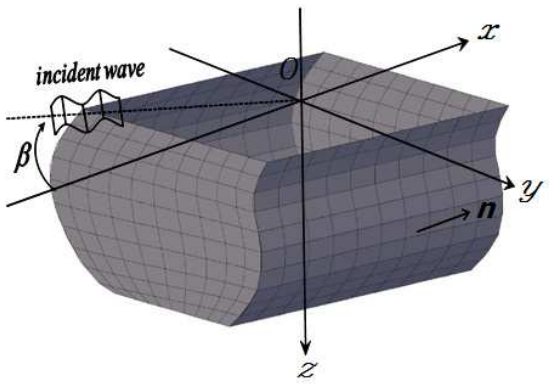

FIGURE 5.1: Coordinate system in the 3D analysis

The origin of the coordinate system is placed at the center of the body and on the undisturbed free surface, and the z-axis is taken positive vertically downward. The water depth is assumed to be infinite. The regular wave is considered to be incoming with incident angle β with respect to the x-axis as shown in Fig. 5.1. Thus $\beta = -90$ degree means the beam wave incoming from the positive y-axis.

Under the assumption of incompressible and inviscid flow with irrotational motion, the velocity potential can be introduced, satisfying Laplace's equation as the governing equation. The boundary conditions are linearized and all oscillatory quantities are assumed to be time-harmonic with circular frequency ω. Applying

superposition principle, the velocity potential can be expressed as a summation of the incident-wave potential ϕ_0 and the disturbance potential ϕ as follows:

$$\Phi(x, y, z, t) = \mathrm{Re}\left[\{\phi_0(x, y, z) + \phi(x, y, z)\}\, e^{i\omega t}\right] \tag{5.1}$$

where ϕ_0 for infinite water depth case can be given explicitly as

$$\phi_0(x, y, z) = \frac{g\zeta_a}{i\omega} e^{-Kz - iK(x\cos\beta + y\sin\beta)} \tag{5.2}$$

with g the acceleration of gravity, ζ_a the amplitude of incident wave, and K the wavenumber given by $K = \omega^2/g$.

Furthermore the disturbance potential ϕ can be decomposed in the following form

$$\phi(x, y, z) = \frac{g\zeta_a}{i\omega}\left[\phi_7(x, y, z) - K\sum_{j=1}^{6}\frac{X_j}{\zeta_a}\phi_j(x, y, z)\right] \tag{5.3}$$

where ϕ_7 denotes the scattering potential in the diffraction problem, and ϕ_j is the radiation potential in the j-th mode of body motion with complex amplitude X_j . In 3D problems, we consider six degrees of freedom in general as shown in Eq. (5.3), but we will focus our attention in this paper on sway ($j = 2$), heave ($j = 3$), and roll ($j = 4$) in following waves, because 3D effects will be discussed through comparison with corresponding 2D results. For the diffraction problem, the sum of $\phi_0 + \phi_7$ is denoted as ϕ_D, which is referred to as the diffraction potential in this study.

The governing equation and boundary conditions to be satisfied can be summarized as follows:

$$[L] \ \nabla^2\phi_j = 0 \quad \text{for } z \geq 0 \tag{5.4}$$

$$[F] \ \frac{\partial\phi_j}{\partial z} + K\phi_j = 0 \text{ on } \ z = 0 \tag{5.5}$$

$$[H] \ \frac{\partial\phi_j}{\partial n} = \begin{cases} n_j \ \ (j = 1 \sim 6) \\ 0 \ \ (j = D) \end{cases} \quad \text{on } S_H \tag{5.6}$$

$$[B] \ \frac{\partial\phi_j}{\partial z} = 0 \text{ as } z \to \infty \tag{5.7}$$

and also an appropriate radiation condition of outgoing waves must be satisfied for $j = 1 \sim 7$. Here S_H denotes the body wetted surface and n_j the j-th component of the normal vector, defined as positive when directing out of the body and into the fluid. These normal vectors are written as follows

$$\left.\begin{array}{l} n_1 = n_x, \quad n_2 = n_y, \quad n_3 = n_z \\ n_4 = yn_z - zn_y, \quad n_5 = zn_z - xnz, \quad n_6 = xn_y - yn_1 \end{array}\right\} \tag{5.8}$$

Assuming the position of the center of gravity G is denoted by (x_g, y_g, z_g), the body boundary condition in radiation case and normal vectors with respect to G for general body case can be written as

$$\frac{\partial\phi_j^G}{\partial n} = n_j^G \tag{5.9}$$

$$\left.\begin{array}{l} n_j^G = n_j \quad \text{for } j = 1 \sim 3 \\ n_4^G = (y - y_g)n_z - (z - z_g)ny = n_4 - y_g n_3 + z_g n_2 \\ n_5^G = (z - z_g)n_x - (x - x_g)nz = n_5 - z_g n_1 + x_g n_3 \\ n_6^G = (x - x_g)n_y - (y - y_g)nx = n_6 - x_g n_2 + y_g n_1 \end{array}\right\} \tag{5.10}$$

So the radiation potential can be transformed as follows

$$\left.\begin{aligned}
\phi_j^G &= \phi_j \quad \text{for } j = 1 \sim 3 \\
\phi_4^G &= \phi_4 - y_g\phi_3 + z_g\phi_2 \\
\phi_5^G &= \phi_5 - z_g\phi_1 + x_g\phi_3 \\
\phi_6^G &= \phi_6 - x_g\phi_2 + y_g\phi_1
\end{aligned}\right\} \tag{5.11}$$

By using Green's theorem, the governing differential equations of the present problem are turned into integral equations on the boundary. That boundary surface can be only the body surface S_H by introducing the free-surface Green function, and the resulting integral equations can be written in the form

$$\begin{aligned}
&C(\mathrm{P})\phi_j + \int\int_{S_H} \phi_j(\mathrm{Q})\frac{\partial}{\partial n_\mathrm{Q}} G(\mathrm{P};\mathrm{Q})dS(\mathrm{Q}) \\
&\qquad = \begin{cases} \displaystyle\int\int_{S_H} n_j(\mathrm{Q})G(\mathrm{P};\mathrm{Q})dS(\mathrm{Q}) & j = 1 \sim 6 \\ \phi_0(\mathrm{P}) & j = D \end{cases}
\end{aligned} \tag{5.12}$$

where $C(\mathrm{P})$ is the solid angle, $\mathrm{P} = (x, y, z)$ is the field point, $\mathrm{Q} = (x', y', z')$ is the integration point on the body surface. $G(\mathrm{P}, \mathrm{Q})$ is the free-surface Green function satisfying the linearized free-surface and radiation conditions, which can be expressed as

$$G(\mathrm{P};\mathrm{Q}) = -\frac{1}{4\pi}\left(\frac{1}{r} + \frac{1}{r_1}\right) - \frac{K}{2\pi}G_W(R, z + z') \tag{5.13}$$

where

$$\left.\begin{matrix} r \\ r_1 \end{matrix}\right\} = \sqrt{(x - x')^2 + (y - y')^2 + (z \mp z')^2} \equiv \sqrt{R^2 + (z \mp z')^2} \tag{5.14}$$

$$G_W(R, z) = -\frac{2}{\pi}\int_0^\infty \frac{k\sin kz + K\cos kz}{k^2 + K^2} K_0(kR)dk - i\pi e^{-Kz}H_0^{(2)}(KR) \tag{5.15}$$

Here $K_0(kR)$ denotes the second kind of modified Bessel function of zero-th order and $H_0^{(2)}(KR)$ the second kind of Hankel function of zero-th order.

5.1.2 Higher-order Boundary Element Method (HOBEM)

In order to attain high accuracy, the integral equation shown above was numerically solved by the Higher-Order Boundary Element Method (HOBEM), described in Kashiwagi [13]. The body surface is discretized into a number of quadrilateral panels. According to the concept of iso-parametric representation, both body surface and unknown velocity potential on each panel are represented with 9-point quadratic shape functions $N_k(\xi,\eta)(k=1\sim 9)$ as follows:

$$(x,y,z)^T = \sum_{k=1}^{9} N_k(\xi,\eta)(x_k,y_k,z_k)^T \tag{5.16}$$

$$\phi(x,y,z) = \sum_{k=1}^{9} N_k(\xi,\eta)\phi_k \tag{5.17}$$

where (x_k,y_k,z_k) are local coordinates at 9-nodal points on a panel under consideration, and likewise ϕ_k denotes the value of the velocity potential (which is to be determined) at 9-nodal points of a panel.

The shape function in Eqs. (5.16) and (5.17) for a quadrilateral panel can be expressed in the form

$$\left.\begin{aligned} N_k &= \frac{1}{4}\xi(\xi+\xi_k)\eta(\eta+\eta_k) \text{ for } k=1\sim 4 \\ N_5 &= \frac{1}{2}\eta(\eta-1)(1-\eta^2), N_6 = \frac{1}{2}\xi(\xi+1)(1-\eta^2) \\ N_7 &= \frac{1}{2}\eta(\eta+1)(1-\eta^2), N_8 = \frac{1}{2}\xi(\xi-1)(1-\eta^2) \\ N_9 &= (1-\xi^2)(1-\eta^2) \end{aligned}\right\} \tag{5.18}$$

where index k denotes the local node number ($k = 1 \sim 9$), as shown in Fig. 5.2.

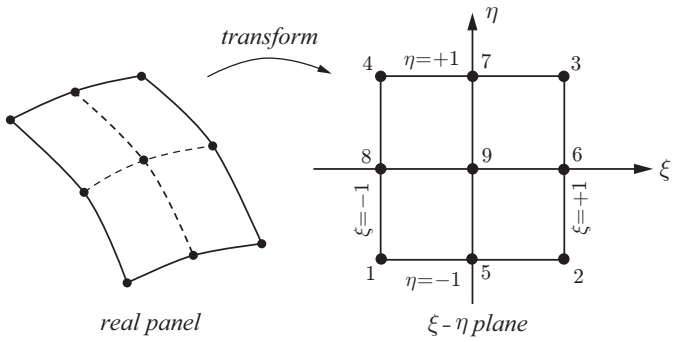

FIGURE 5.2: Quadrilateral 9-node Lagrangian element

The normal vector on the body surface (each panel) can be computed with differentiation of the shape function as follows:

$$\boldsymbol{n} = \frac{\boldsymbol{a} \times \boldsymbol{b}}{|\boldsymbol{a} \times \boldsymbol{b}|},\ \boldsymbol{a} = \left(\frac{\partial x}{\partial \xi}, \frac{\partial y}{\partial \xi}, \frac{\partial z}{\partial \xi}\right),\ \boldsymbol{b} = \left(\frac{\partial x}{\partial \eta}, \frac{\partial y}{\partial \eta}, \frac{\partial z}{\partial \eta}\right) \tag{5.19}$$

Through a series of substitution, finally the bounday integral equations can be recast in a series of algebraic equations for the velocity potentials at nodal points consisting of panels. The results can be expressed in the form

$$C_m \phi_m + \sum_{l=1}^{NT} D_{ml} \phi_l = \begin{cases} \displaystyle\sum_{n=1}^{N} S_{mn}^j & j = 1 \sim 6,\ m = 1 \sim NT \\ \phi_0(\mathrm{P}_m) \end{cases} \tag{5.20}$$

where

$$D_{ml} = \int\int_{S_H} N_k(\xi, \eta) \frac{\partial G(\mathrm{P}_m; \mathrm{Q})}{\partial n_Q} |J(\xi, \eta)| d\xi d\eta \tag{5.21}$$

$$S_{mn}^j = \int\int_{S_H} n_j(\mathrm{Q}) G(\mathrm{P}_m; \mathrm{Q}) |J(\xi, \eta)| d\xi d\eta \tag{5.22}$$

and index n denotes the serial n-th panel, index m the global serial number of nodal points, and $l = (n, k)$ is also the serial number of nodal points associated

with (to be computed from) the k-th local node within the n-th panel. $|J(\xi,\eta)|$ in Eqs. (5.21) and (5.22) denotes the Jacobian in the variable transformation. NT denotes the total number of nodal points and thus Eq. (5.20) is a linear system of simultaneous equations with dimension of $NT \times NT$ for the unknown velocity potentials at nodal points. The solid angle C_m in Eq. (5.20) is computed numerically by considering the equi-potential condition that a uniform potential applied over a closed domain produces no flux and thus zero normal velocities over the entire boundary.

The free-surface Green function, given by Eq. (5.15), can be computed efficiently by combining several expressions such as the power series, asymptotic expansions, and recursion formulae; its subroutine is available in Kashiwagi et al. [11].

In actual numerical computations, a few additional field points are considered on the interior free surface of a floating body for the purpose of removing the irregular frequencies. At these field points, the value of solid angle C_m in Eq. (5.20) must be zero; this technique is adopted following the idea of Haraguchi and Ohmatsu [12] as used in 2D problems. The resultant over-constraint simultaneous equations are solved with the least-square method.

5.1.3 Hydrodynamic Forces

Once the velocity potentials on the body surface are determined, it is straightforward to compute the hydrodynamic forces. Similar to 2D case, the hydrodynamic forces are obtained from integration of pressure multiplied by ith component of the normal vector. For radiation problem, the hydrodynamic force working in i-th direction is written as

$$F_i = -\rho(i\omega)^2 \sum_{j=1}^{6} X_j \int\int_{S_H} \phi_j n_i dS = \sum_{j=1}^{6} T_{ij} X_j \tag{5.23}$$

where

$$T_{ij} = (i\omega)^2 A_{ij} - (i\omega)B_{ij} = -\rho(i\omega)^2 \int\int_{S_H} \phi_j n_i dS \tag{5.24}$$

The transfer function T_{ij} in Eq. (5.24) is expressed with respect to origin of the coordinate system shown in Fig. 5.1. This quantity can be expressed with respect to the center of gravity G as follows

$$T_{ij}^G = -\rho(i\omega)^2 \int\int_{S_H} \phi_j^G n_i^G dS = (i\omega)^2 A_{ij}^G - (i\omega)B_{ij}^G \tag{5.25}$$

when $i = 1 \sim 3$ and $j = 1 \sim 3$, it is known that $T_{ij}^G = T_{ij}$. For other cases, they can be written as follows

- when $i = 1 \sim 3$

$$T_{i4}^G = -\rho(i\omega)^2 \int\int_{S_H} (\phi_4 - y_g\phi_3 + z_g\phi_2) n_i dS = T_{i4} - y_g T_{i3} + z_g T_{i2} \tag{5.26}$$

$$T_{i5}^G = -\rho(i\omega)^2 \int\int_{S_H} (\phi_5 - z_g\phi_1 + x_g\phi_3) n_i dS = T_{i5} - z_g T_{i1} + x_g T_{i3} \tag{5.27}$$

$$T_{i6}^G = -\rho(i\omega)^2 \int\int_{S_H} (\phi_6 - x_g\phi_2 + y_g\phi_1) n_i dS = T_{i6} - x_g T_{i2} + y_g T_{i1} \tag{5.28}$$

- when $i = 4$ and $j = 4 \sim 6$

$$\begin{aligned} T_{44}^G &= -\rho(i\omega)^2 \int\int_{S_H} \phi_4^G (n_4 - y_g n_3 + z_g n_2) dS, \quad \phi_4^G = \phi_4 - y_g\phi_3 + z_g\phi_2 \\ &= T_{44} - y_g T_{43} + z_g T_{42} - y_g T_{34}^G + z_g T_{24}^G \end{aligned} \tag{5.29}$$

$$\begin{aligned} T_{45}^G &= -\rho(i\omega)^2 \int\int_{S_H} \phi_5^G (n_4 - y_g n_3 + z_g n_2) dS, \quad \phi_5^G = \phi_5 - z_g\phi_1 + x_g\phi_3 \\ &= T_{45} - z_g T_{41} + x_g T_{43} - y_g T_{35}^G + z_g T_{25}^G \end{aligned} \tag{5.30}$$

$$\begin{aligned} T_{46}^G &= -\rho(i\omega)^2 \int\int_{S_H} \phi_6^G (n_4 - y_g n_3 + z_g n_2) dS, \quad \phi_6^G = \phi_6 - x_g\phi_2 + y_g\phi_1 \\ &= T_{46} - x_g T_{42} + y_g T_{41} - y_g T_{36}^G + z_g T_{26}^G \end{aligned} \tag{5.31}$$

- when $i = 5$ and $j = 4 \sim 6$

$$T_{54}^G = -\rho(i\omega)^2 \int\int_{S_H} \phi_4^G (n_5 - z_g n_1 + x_g n_3) dS, \quad \phi_4^G = \phi_4 - y_g \phi_3 + z_g \phi_2$$
$$= T_{54} - y_g T_{53} + z_g T_{52} - z_g T_{14}^G + x_g T_{34}^G \tag{5.32}$$
$$T_{55}^G = -\rho(i\omega)^2 \int\int_{S_H} \phi_5^G (n_5 - z_g n_1 + x_g n_3) dS, \quad \phi_5^G = \phi_5 - z_g \phi_1 + x_g \phi_3$$
$$= T_{55} - z_g T_{51} + x_g T_{53} - z_g T_{15}^G + x_g T_{35}^G \tag{5.33}$$
$$T_{56}^G = -\rho(i\omega)^2 \int\int_{S_H} \phi_6^G (n_5 - z_g n_1 + z_g n_3) dS, \quad \phi_6^G = \phi_6 - x_g \phi_2 + y_g \phi_1$$
$$= T_{56} - x_g T_{52} + y_g T_{51} - z_g T_{16}^G + x_g T_{36}^G \tag{5.34}$$

- when $i = 6$ and $j = 4 \sim 6$

$$T_{64}^G = -\rho(i\omega)^2 \int\int_{S_H} \phi_4^G (n_6 - x_g n_2 + y_g n_1) dS, \quad \phi_4^G = \phi_4 - y_g \phi_3 + z_g \phi_2$$
$$= T_{64} - y_g T_{63} + z_g T_{62} - x_g T_{24}^G + y_g T_{14}^G \tag{5.35}$$
$$T_{65}^G = -\rho(i\omega)^2 \int\int_{S_H} \phi_5^G (n_6 - x_g n_2 + y_g n_1) dS, \quad \phi_5^G = \phi_5 - z_g \phi_1 + x_g \phi_3$$
$$= T_{65} - z_g T_{61} + x_g T_{63} - x_g T_{25}^G + x_g T_{15}^G \tag{5.36}$$
$$T_{66}^G = -\rho(i\omega)^2 \int\int_{S_H} \phi_6^G (n_6 - x_g n_2 + y_g n_1) dS, \quad \phi_6^G = \phi_6 - x_g \phi_2 + y_g \phi_1$$
$$= T_{66} - x_g T_{62} + y_g T_{61} - z_g T_{26}^G + x_g T_{16}^G \tag{5.37}$$

From diffraction case, the wave exciting force E_i with respect to origin O can be obtained as follows

$$E_i = \rho g \zeta_a \int\int_{S_H} \phi_D n_i dS \tag{5.38}$$

Its reference is transformed to the center of gravity G which gives

$$E_i^G = \rho g \zeta_a \int\int \phi_D n_i^G dS \tag{5.39}$$

The explicit expression can be written for different values of i as follows

- when $i = 1 \sim 3$

$$\rho g \zeta_a \int \int_{S_H} \phi_D n_i^G dS = E_i \tag{5.40}$$

- when $i = 4 \sim 6$

$$E_4^G = \rho g \zeta_a \int \int \phi_D (n_4 - y_g n_3 + z_g n_2) dS = E_4 - y_g E_3 + z_g E_2 \tag{5.41}$$

$$E_5^G = \rho g \zeta_a \int \int \phi_D (n_5 - z_g n_1 + x_g n_3) dS = E_5 - z_g E_1 + x_g E_3 \tag{5.42}$$

$$E_6^G = \rho g \zeta_a \int \int \phi_D (n_6 - x_g n_2 + y_g n_1) dS = E_6 - x_g E_2 + y_g E_1 \tag{5.43}$$

From the hydrostatic pressure, the restoring force with respect to the center of gravity can be obtained as follows

$$S_i^G = -\rho g \int \int_{S_H} \left\{ X_3^G + (y - y_g) X_4^G - (x - x_g) X_5^G \right\} n_i^G dS \tag{5.44}$$

which is shown in nondimensionalized form as follows

$$S_i^G = -\rho g \zeta_a b^2 \epsilon_i \left[\frac{X_3^G}{\zeta_a} C_{i3} + \frac{X_4^G b}{\zeta_a} C_{i4} + \frac{X_5^G b}{\zeta_a} C_{i5} \right] \tag{5.45}$$

where

$$\left.\begin{aligned} C_{i3} &= \int \int_{S_H} n_i^G dS \\ C_{i4} &= \int \int_{S_H} (y - y_g) n_i^G dS \\ C_{i5} &= \int \int_{S_H} (-x + x_g) n_i^G dS \end{aligned}\right\} \tag{5.46}$$

Because it exists only when $i = 3 \sim 5$, so we write the following normal vectors

$$\left.\begin{aligned} n_3^G &= n_z \\ n_4^G &= (y - y_g)n_z - (z - z_g)n_y \\ n_5^G &= (z - z_g)n_x - (x - x_g)n_z \end{aligned}\right\} \tag{5.47}$$

Using Gauss's theorem, Eq. (5.46) can be written as

- for $i = 3$

$$C_{33} = \int\int_{S_H} n_3 dS = \int\int_{S_F} dxdy = A_w \tag{5.48}$$

$$C_{34} = \int\int_{S_H} (y - y_g)n_3 dS = \int\int_{S_F} (y - y_g)dxdy = (y_F - y_g)A_w \tag{5.49}$$

$$C_{35} = \int\int_{S_H} (-x + x_g)n_3 dS = \int\int_{S_F} (-x + x_g)dxdy = -(x_F - x_g)A_w \tag{5.50}$$

- for $i = 4$

$$\begin{aligned} C_{43} &= \int\int_{S_H} \{(y - y_g)n_z - (z - z_g)n_y\}\, dS \\ &= \int\int_{S_F} (y - y_g)dxdy = C_{34} \end{aligned} \tag{5.51}$$

$$\begin{aligned} C_{44} &= \int\int_{S_H} (y - y_g)\{(y - y_g)n_z - (z - z_g)n_y\}\, dS \\ &= \int\int_{S_F} (y - y_g)^2 dxdy - \int\int\int_V (z - z_g)dV \\ &= \int\int_{S_F} y^2 dxdy + (-2y_g y_f + y_g^2)A_w + (z_g - z_B)V \end{aligned} \tag{5.52}$$

$$
\begin{aligned}
C_{45} &= -\int\int_{S_H} (x-x_g)\left\{(y-y_g)n_z - (z-z_g)n_y\right\} dS \\
&= \int\int_{S_F} (x-x_g)(y-y_g)dxdy \\
&= \int\int_{S_F} xydxdy + (x_g y_f + x_F y_g - x_g y_g)A_w
\end{aligned} \tag{5.53}
$$

- for $i = 5$

$$
\begin{aligned}
C_{53} &= \int\int_{S_H} \left\{(z-z_g)n_x - (x-x_g)n_z\right\} dS \\
&= -\int\int_{S_F} (x-x_g)dxdy = -(x_F - x_g)A_w = C_{35}
\end{aligned} \tag{5.54}
$$

$$
\begin{aligned}
C_{54} &= \int\int_{S_H} (y-y_g)\left\{(z-z_g)n_x - (x-x_g)n_z\right\} dS \\
&= -\int\int_{S_F} (x-x_g)(y-y_g)dxdy = C_{45}
\end{aligned} \tag{5.55}
$$

$$
\begin{aligned}
C_{55} &= -\int\int_{S_H} (x-x_g)\left\{(z-z_g)n_x - (x-x_g)n_z\right\} dS \\
&= -\int\int\int_V (z-z_g)dV + \int\int_{S_F} (x-x_g)^2 dxdy \\
&= \int\int_{S_F} x^2 dxdy + (-2x_g x_f + x_g^2)A_w + (z_g - z_B)V
\end{aligned} \tag{5.56}
$$

In above expressions, variables that need to be known are as follows

$$
\left.
\begin{aligned}
V &= \int\int\int_V dV, \quad y_B(=y_g), z_B, y_F \\
A_w &= \int\int_{S_F} dxdy, \int\int_{S_F} y^2 dxdy, \int\int_{S_F} x^2 dxdy
\end{aligned}
\right\} \tag{5.57}
$$

The same notations for body cross section with the ones used in 2D case (refer to Fig. 2.8) are used in above expressions. For the calculation of a single symmetric body which is shown in Fig. 5.1 as an example, we have $x_F = x_g = 0$, while

z_g is obtained from input data. Denoting the position of center of buoyancy as $(0, y_B, z_B)$ and cross section area as S, we have

$$\left.\begin{aligned} S &= \frac{1}{2}\sum_{j=1}^{N}(y_j - y_{j+1})(z_j + z_{j+1}) \\ Sy_B &= \frac{1}{6}\sum_{j=1}^{N}(y_j - y_{j+1})\left[z_j(2y_j + y_{j+1} + z_{j+1}(2y_{j+1} + y_j)\right] \\ Sz_B &= \frac{1}{6}\sum_{j=1}^{N}(z_{j+1} - z_j)\left[y_j(2z_j + z_{j+1} + y_{j+1}(2z_{j+1} + z_j)\right] \\ B &= y_a - y_b, \quad \frac{1}{2}(y_a + y_b), \quad y_g = y_B \end{aligned}\right\} \tag{5.58}$$

Using those data, the quantities in Eq. (5.57) can be obtained as follows

$$\left.\begin{aligned} &V = SL, \quad A_w = BL, \\ &\int\int_{S_F} y^2 dxdy = \frac{L}{3}(y_a^3 - y_b^3), \\ &\int\int_{S_F} x^2 dxdy = \frac{L^3}{12}B = \frac{L^2}{12}BA_w \end{aligned}\right\} \tag{5.59}$$

where L is the length of the body. Using (5.59), the hydrostatic force and moment can be written as

$$\left.\begin{aligned} &C_{33} = A_w, \quad C_{34} = (y_F - y_g)A_w, \quad C_{35} = 0 \\ &C_{43} = C_{34}, \quad C_{45} = 0, \quad C_{53} = 0, \quad C_{54} = 0 \\ &C_{44} = V(z_g - z_B) + A_w\left\{y_g^2 - 2y_g y_F + \frac{1}{3}(y_a^2 + y_a y_b + y_b^2)\right\} \\ &C_{55} = V(z_g - z_B) + A_w\frac{1}{12}L^2 \end{aligned}\right\} \tag{5.60}$$

We can write the combination of the hydrodynamic force expressions above as follows

$$\overline{F} = \rho g \zeta_a b^2 \epsilon_i F_i^G \tag{5.61}$$

where

$$F_i^G = E_i^G + Kb\sum_{j=1}^{6}\frac{X_j^G\epsilon_j}{\zeta_a}T_{ij}^G - \sum_{j=3}^{5}\frac{X_j^G\epsilon_j}{\zeta_a}C_{ij} \tag{5.62}$$

which can be written in other forms as follows

$$\begin{aligned} -\omega^2\sum_{j=1}^{6}X_j^G m_{ij}\delta_{ij} &= \overline{F} \\ -Kb\sum_{j=1}^{6}\frac{X_j^G\epsilon_j}{\zeta_a}\left(\frac{m_{ij}}{\rho a^3\epsilon_i\epsilon_j}\right)\delta_{ij} &= F_i^G \end{aligned} \tag{5.63}$$

In the final form can be written as

$$\sum_{j=1}^{6}X_j^G\left\{-K\left(M_{ij}\delta_{ij}+F_{ij}^G\right)+C_{ij}^G\right\} = E_i^G \quad i=1\sim 6 \tag{5.64}$$

where

$$M_{ij} = \frac{m_{ij}}{\rho b^3\epsilon_i\epsilon_j} \tag{5.65}$$

Superscript G means quantities with respect to the center of gravity. M_{ij} denotes the genralized mass matrix, δ_{ij} is the Kroenecker's delta, and C_{ij}^G is the restoring-force coefficients due to the static pressure. By solving these coupled motion equations, the complex motion amplitude X_j^G can be determined and then the corresponding complex amplitude with respect to the origin of the coordinate system $X_j(j=1\sim 6)$ can be obtained from

$$\left.\begin{aligned} X_j &= X_j^G + \epsilon_{jkl}(x_G)_k X_{l+3}^G \\ X_{j+3} &= X_{j+3}^G \end{aligned}\right\}(j=1\sim 3) \tag{5.66}$$

where ϵ_{jkl} denotes the alternating tensor for the outer product of vectors and $(x_G)_k$ $(k=1\sim 3)$ the ordinates of the center of gravity.

The numerical accuracy can be confirmed by checking the Haskind-Newman relation for the wave-exciting force and the energy-conservation relation for the damping coefficient. These relations are expressed as

$$E_j = \rho g \zeta_a H_j(K, \beta) \tag{5.67}$$

$$B_{ij} = \frac{\rho \omega K}{4\pi} \mathrm{Re} \int_0^{2\pi} H_i(K, \theta) H_j^*(K, \theta) d\theta \tag{5.68}$$

where H_j denotes the so-called Kochin function in the radiation problem, expressed as

$$H_j(K, \theta) = \int \int_{S_H} \left(\frac{\partial \phi_j}{\partial n} - \phi_j \frac{\partial}{\partial n} \right) e^{-Kz - iK(x \cos\theta + y \sin\theta)} dS \tag{5.69}$$

In terms of the Kochin function, the wave drift forces in the $x-$ and $y-$axes as described in Maruo [14] and the drift moment about the $z-$axis in Newman [15] can be computed. The formulae for the first two components are written as

$$\left.\begin{aligned} \bar{F}_x &= \frac{\rho g \zeta_a^2}{8\pi} K \int_0^{2\pi} |H(K, \theta)|^2 (\cos\beta - \cos\theta) \, d\theta \\ \bar{F}_y &= \frac{\rho g \zeta_a^2}{8\pi} K \int_0^{2\pi} |H(K, \theta)|^2 (\sin\beta - \sin\theta) \, d\theta \end{aligned}\right\} \tag{5.70}$$

where

$$H(K, \theta) = H_7(K, \theta) - K \sum_{j=1}^{6} \frac{X_j}{\zeta_a} H_j(K, \theta) \tag{5.71}$$

$$H_7(K, \theta) = - \int \int_{S_H} \phi_D \frac{\partial}{\partial n} e^{-Kz - iK(x \cos\theta + y \sin\theta)} dS \tag{5.72}$$

5.1.4 Wave Elevation on the Free Surfaces

The wave elevation on the free surface in the linear theory can be computed from

$$\frac{\zeta(x, y)}{\zeta_a} = \phi_0(x, y, 0) + \phi_7(x, y, 0) - K \sum_{j=1}^{6} \frac{X_j}{\zeta_a} \phi_j(x, y, 0) \tag{5.73}$$

where the velocity potentials due to disturbance by a floating body can be computed from

$$\phi_7(\mathrm{P}) = -\int\int_{S_H} \phi_D(\mathrm{Q}) \frac{\partial}{\partial n_Q} G(\mathrm{P};\mathrm{Q}) dS(\mathrm{Q}) \tag{5.74}$$

$$\phi_j(\mathrm{P}) = -\int\int_{S_H} \left\{ n_j(\mathrm{Q}) - \phi_j \frac{\partial}{\partial n_Q} \right\} G(\mathrm{P};\mathrm{Q}) dS(\mathrm{Q}) \tag{5.75}$$

where $\mathrm{P} = (x, y, 0)$ is a point on the free surface.

In HOBEM, these velocity potentials can be computed by using the shape function and the solutions of the velocity potentials at nodal points. The integrals in Eqs. (5.74) and (5.75) can be evaluated by summation over all panels, on which element computations can be done using the same scheme for the coefficients shown in Eqs. (5.21) and (5.22), with the calculation point P placed on the free surface.

In this study, we are concerned with the transmission and reflection waves by a floating breakwater. The transmission wave is defined by the wave in the lee side, propagating in the same direction as that of the incident wave. On the other hand, the reflection wave must be defined as the wave in the weather side, propagating to the opposite direction. Thus the incident-wave term $\phi_0(x, y, 0)$ in Eq. (5.73) is subtracted from Eq. (5.73) in numerical computations for the reflection wave.

5.2 Computation Results and Discussion

Based on the 2D shape obtained in previous chapter, a 3D model shape is constructed by extruding it in the longitudinal direction as shown in Fig. 5.3. The transverse section shape is the same as that in Fig. 4.5 and uniform in the longitudinal x-direction with its length denoted as L.

In 3D computations based on HOBEM, following the 2D analysis, half of the maximum breadth ($b = B/2$) is used for nondimensionalization. The incident

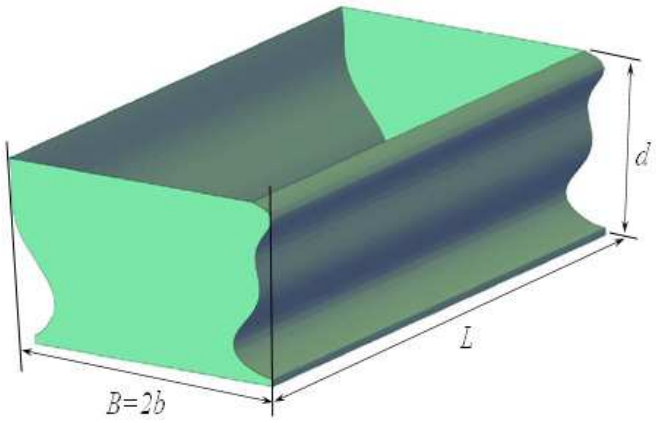

FIGURE 5.3: 3D model shape

angle β of regular incoming wave is set equal to $\beta = -90$ deg. so that the situation corresponds to the 2D case and the results for the body motions and the reflection and transmission wave coefficients can be compared with 2D results; thereby 3D effects on those quantities can be discussed.

Unlike 2D case, the wave amplitude in 3D results may vary depending on the location on the free surface. Thus 3 different positions along the y-axis (centerline of the body) are considered for the wave measurement. The distance of these positions from the origin of the coordinate system is taken equal to $y/b = 4$, 10, and 18 for the reflection wave and $y/b = -4$, -10, and -18 for the transmission wave. (Note that the incident-wave component is subtracted from Eq. (5.73) in the definition of the reflection wave.)

In order to investigate 3D effects depending on the longitudinal length of the body, we have computed for 3 different body lengths; those are L/B=2, 8, and 20. The hydrodymnamic forces are computed, but discussion in this study will be focused on the difference between 2D and 3D results in the amplitude of body motions and the reflection and transmission wave coefficients. In numerical computations, only half of the body was discretized with the symmetry relation with respect to x taken into account. Then to keep sufficient accuracy, a larger number of panels was used, although the results of HOBEM are relatively very accurate.

Specifically, the total number of panels used is 408 for $L/B = 2$, 638 for $L/B = 8$, and 1098 for $L/B = 20$. One panel consists of 9 nodal points and thus the total number of unknowns was 1689, 2629, and 4509 for L/B =2, 8, and 20, respectively. As already described, the numerical accuracy was checked through the Haskind-Newman and energy-conservation relations and found to be very satisfactory with these panels and unknowns.

Computed results for a 3D body with $L/B = 2$ are shown in Fig. 5.4 for the amplitude of body motions and in Fig. 5.5 for the reflection and transmission waves. Figs. 5.5 (a) and 5.5 (b) are for the diffraction problem and Figs. 5.5 (c) and 5.5 (d) are for the case of all motions free.

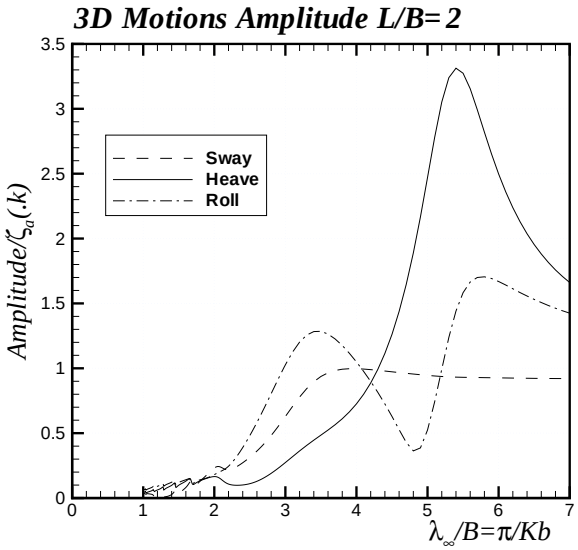

FIGURE 5.4: Body motion amplitudes of 3D model for $L/B = 2$

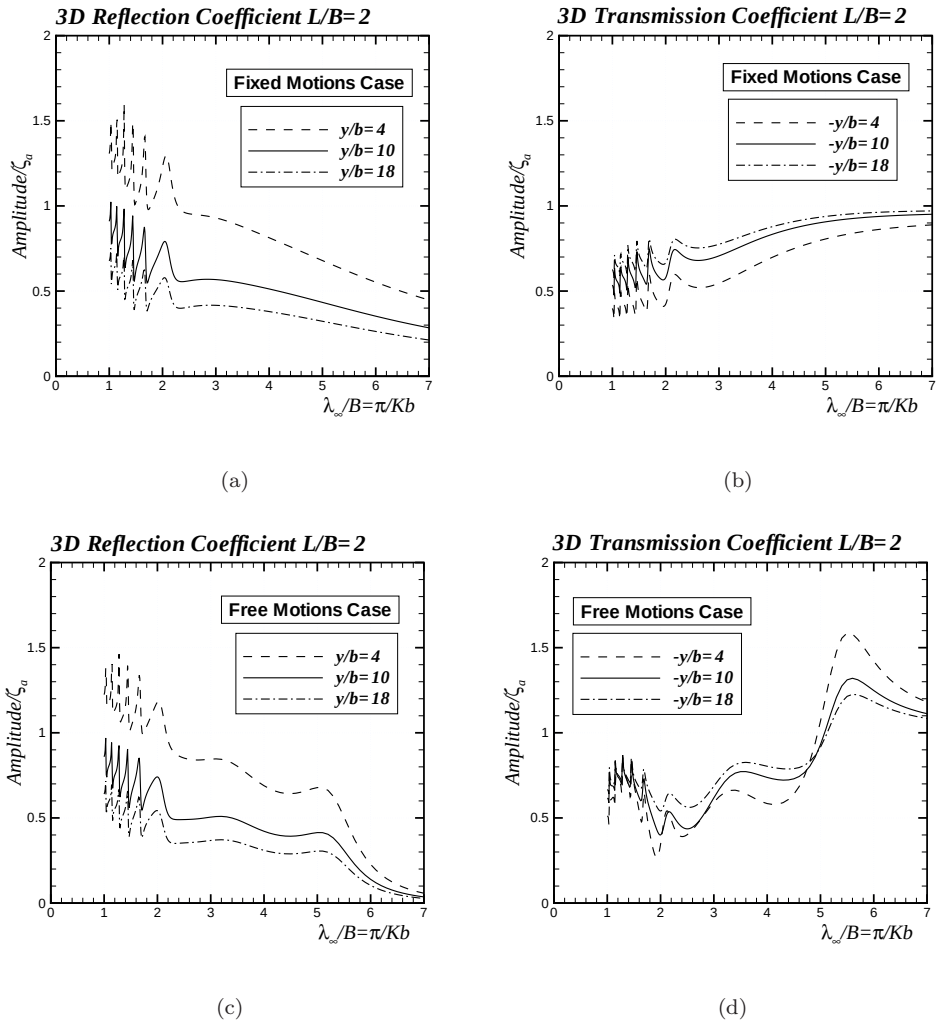

FIGURE 5.5: 3D Reflection (left) and transmission (right) wave coefficients for $L/B = 2$: (a) (b) for fixed motion case, (c) (d) for free motion case

From Fig. 5.4 we can see that the body motions show very similar trend to the 2D results shown in Fig. 4.8, but the amplitude particularly in heave is different. On the other hand, the wave amplitudes shown in Fig. 5.5 are very much different from those by the 2D analysis shown in Figs. 4.6 and 4.7. Furthermore, the wave amplitudes in 3D results are dependent largely on the measurement position. We can envisage that the incident wave is diffracted around the longitudinal tip side of the body and the wave field on the free surface is totally three dimensional.

It should be noted that regular fluctuation in the short wavelength region can be observed. In order to resolve this fluctuation, computations have been performed at dense points of the wavelength with very small interval, and we found that

this fluctuation was caused by the so-called irregular frequencies. As described in the numerical method, zero value of the velocity potential was specified on some interior free-surface points to get rid of the irregular frequencies. However, the results show that this method is not effective for 3D problems. Since computations are conducted at dense wavelengths in the present study, a mean line of this regular fluctuation may be considered as expected results and this fluctuation in the short wavelength region may be not a fatal problem in discussing 3D effects.

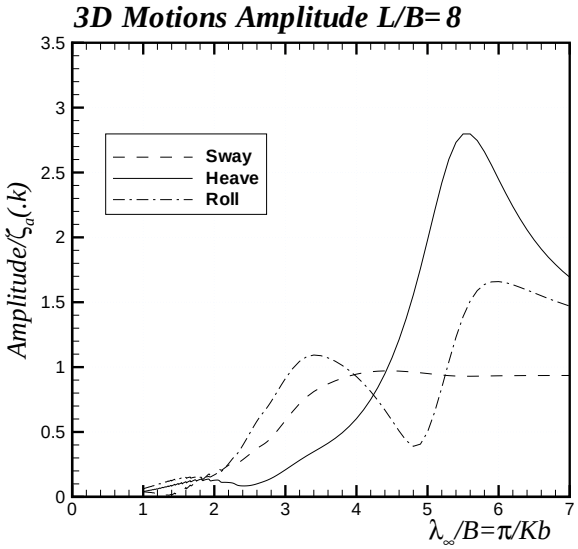

FIGURE 5.6: Body motion amplitudes of 3D model for $L/B = 8$

Computed results for a longer body of $L/B = 8$ are shown in Figs. 5.6 and 5.7 for the amplitudes of body motions and reflection and transmission waves, respectively. Looking at the motion amplitudes in Fig. 5.6 and comparing with Fig. 4.8, we can see that all modes of motion become almost the same not only in the trend but also in the magnitude. This implies that 3D effects on hydrodynamic forces are small enough if the length ratio of the body is taken up to $L/B = 8$.

However, the wave amplitudes are still different from the 2D results, although the global trend becomes similar. For instance, for the case of fixed motions, the reflection wave is large and its coefficient is roughly equal to 1.0, and the transmission wave coefficient is smaller than 0.5. We can also see that, depending

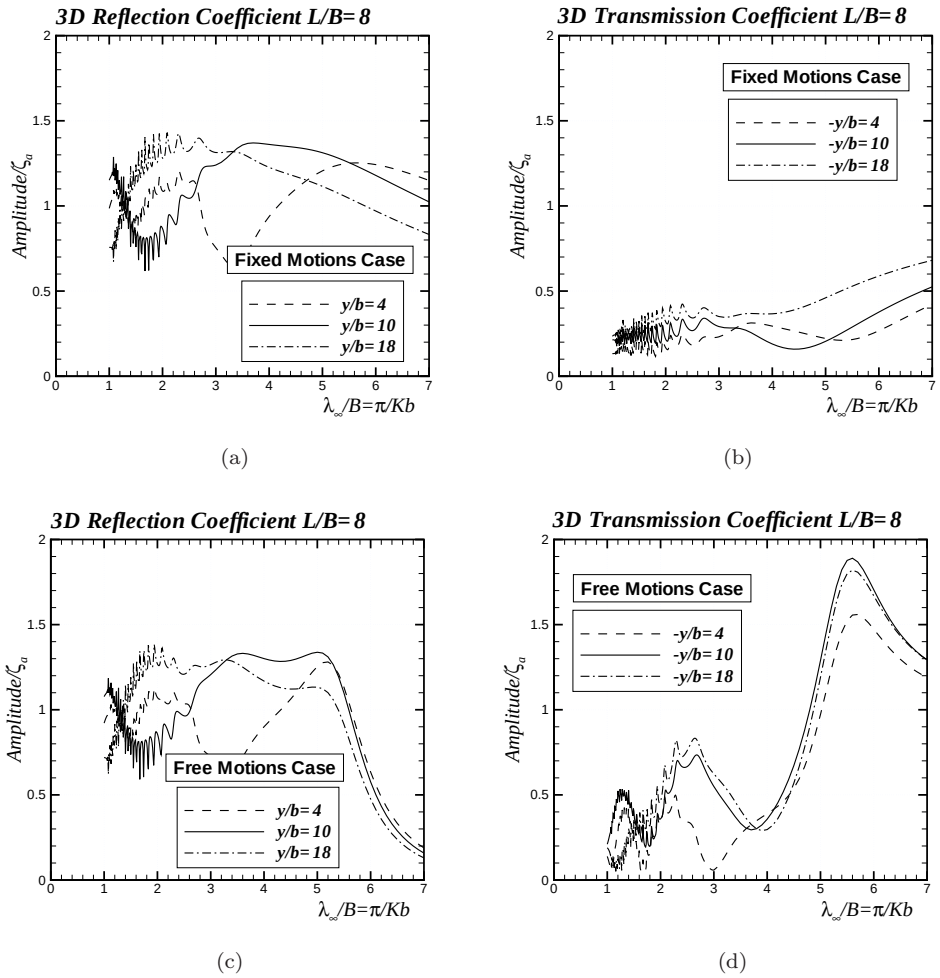

FIGURE 5.7: 3D Reflection (left) and transmission (right) wave coefficients for $L/B = 8$: (a) (b) for fixed motion case, (c) (d) for free motion case

on the position and wavelength, the wave amplitude coefficient becomes larger than 1.0, which should be attributed to 3D effects in the free-surface wave.

In order to see whether more similar results to those in the 2D analysis would be obtained for a longer body, the body length was increased further to $L/B = 20$. Obtained results for the body motions and the reflection and transmission waves are shown in Figs. 5.8 and 5.9, respectively. The amplitudes of body motions are unchanged from the case of $L/B = 8$. However, the results of wave amplitudes are still different but become similar further to the 2D results.

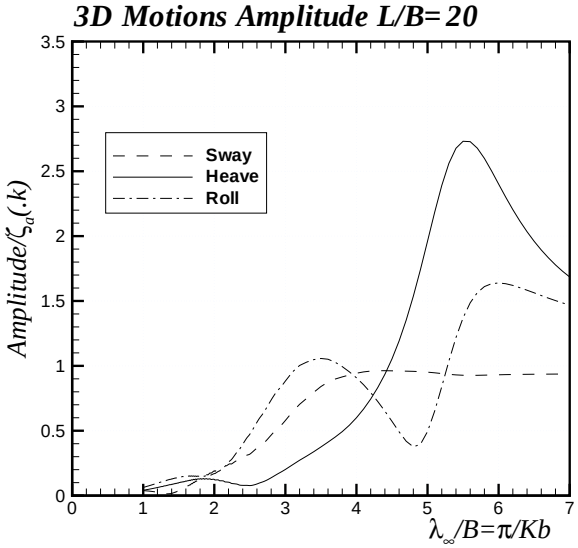

FIGURE 5.8: Body motion amplitudes of 3D model for $L/B = 20$

Although the wave amplitude is still dependent on the position of measurement, the reflection wave coefficient fluctuates around 1.0 and decreases at wavelengths greater than $\lambda/B > 5.5$ for the free-motion case, which is the same in trend as the 2D results. Nevertheless, we can realize that 3D effects are large on the wave amplitude on the free surface even for a longer body of $L/B = 20$.

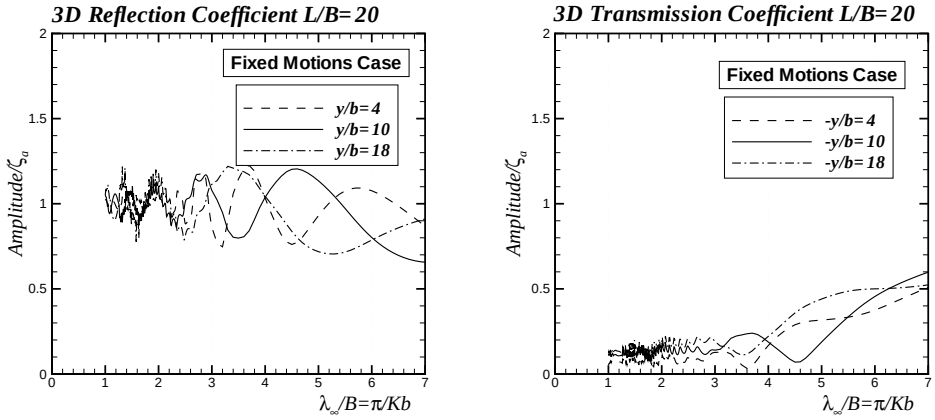

(a) (b)

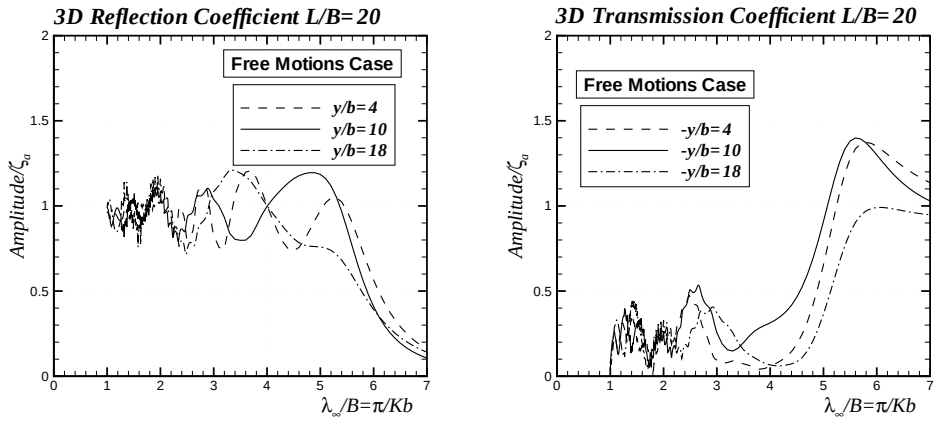

(c) (d)

FIGURE 5.9: 3D Reflection (left) and transmission (right) wave coefficients for $L/B = 20$: (a) (b) for fixed motion case, (c) (d) for free motion case

In order to observe the spatial variation of the free-surface wave around a floating breakwater, numerical computations for the bird's-eye view of the wave field were performed for typical wavelengths; that is, $\lambda/B = 3.0$ and $\lambda/B = 6.0$. Computed results for a short-length body of $L/B = 2$ are shown in Fig. 5.10, where 5.10 (a) and 5.10 (b) are for $\lambda/B = 3.0$ and 5.10 (c) and 5.10 (d) are for $\lambda/B = 6.0$. Both cases of fixed and free motions are computed and shown.

These results are only for the real part (i.e. at time instant $t = 0$) of the total wave elevation. Therefore it may be difficult to distinguish the reflected and incident waves in the weather side, whereas in the lee side we can directly see the spatial distribution of transmitted wave and its correspondence to the results measured at 3 selected points along the $y-$axis (which are shown in Fig. 5.9 for the case of $L/B = 2$).

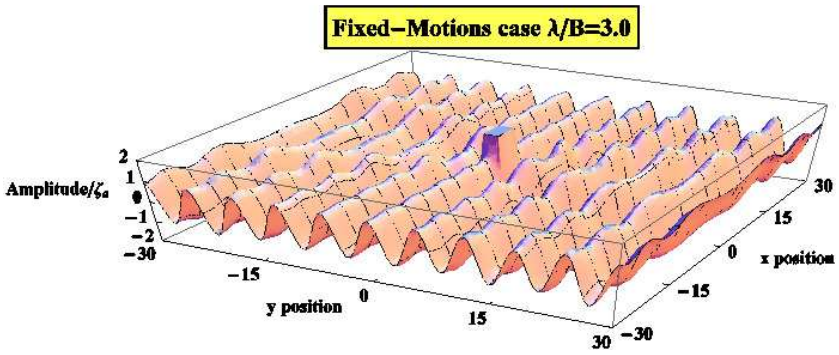

(a)

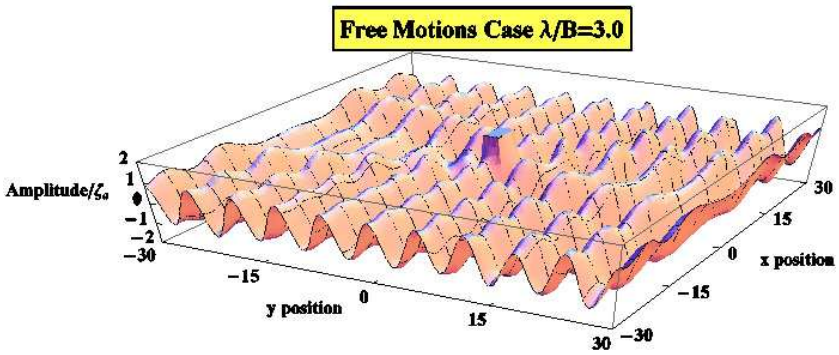

(b)

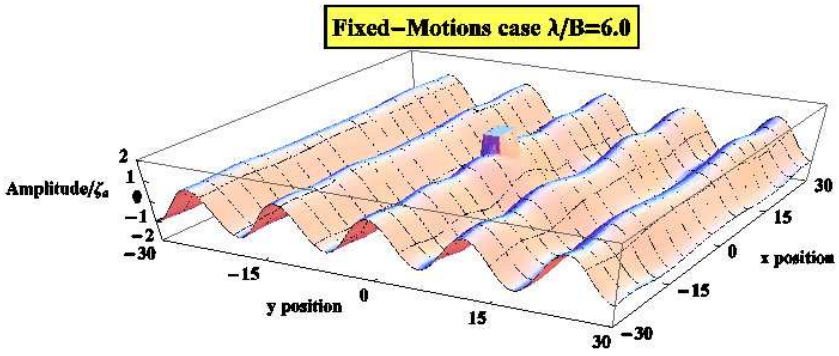

(c)

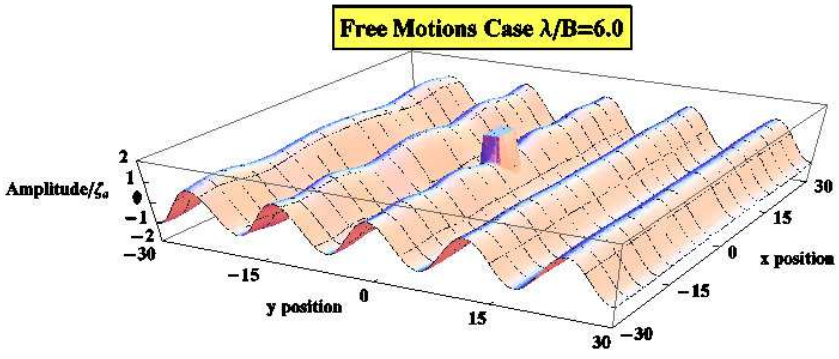

(d)

FIGURE 5.10: Bird's-eye view of 3D wave field around a body of $L/B = 2$ for wavelength of λ/B=3.0 and 6.0

We can see from Fig. 5.10 that the wave is relatively uniform for $\lambda/B = 6.0$ but scattered by the body for $\lambda/B = 3.0$ and the resulting wave pattern becomes three dimensional.

Computed results for a longer body of $L/B = 20$ are shown in Fig. 5.11. Like above, 5.11(a) and 5.11(b) are for $\lambda/B = 3.0$ and 5.11(c) and 5.11(d) are for $\lambda/B = 6.0$, and both cases of fixed and free motions are shown to observe the effect of body motions.

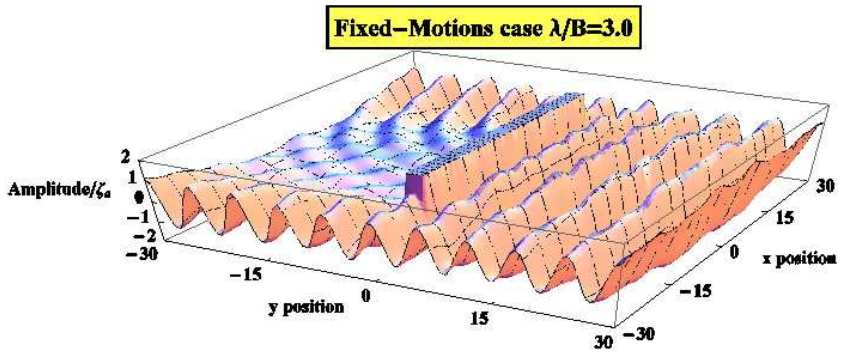

(a)

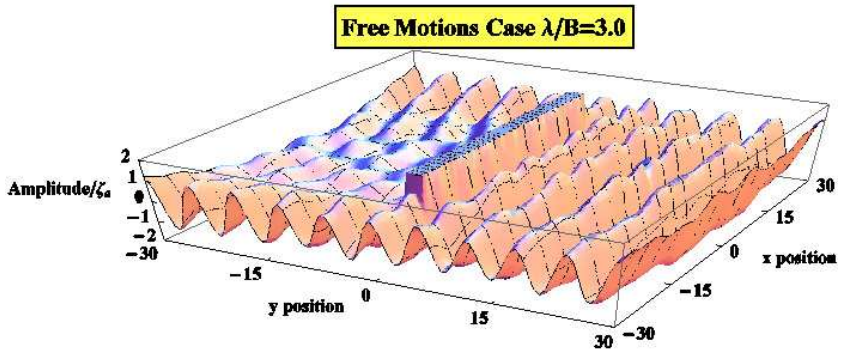

(b)

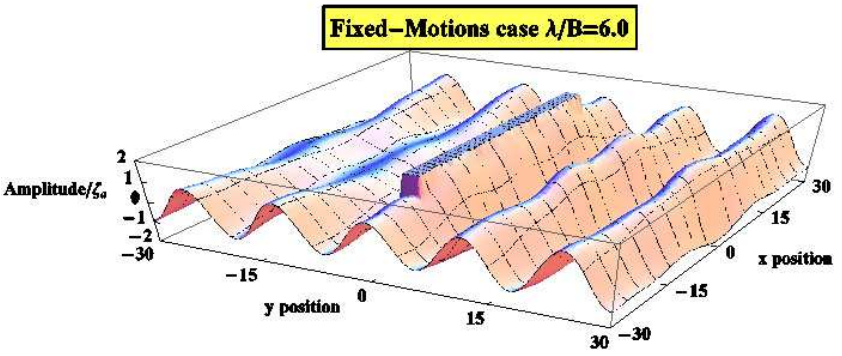

(c)

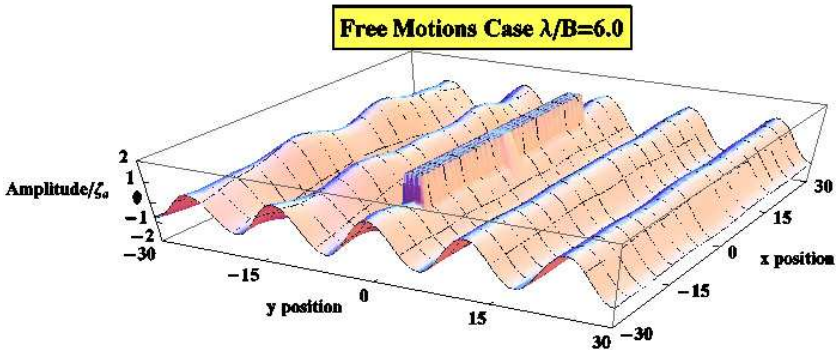

(d)

FIGURE 5.11: Bird's-eye view of 3D wave field around a body of $L/B = 20$ for wavelength of λ/B=3.0 and 6.0

Looking at the wave in the lee side, we can confirm the correspondence to the results in Fig. 5.9 measured at 3 different points along the y-axis. We can see that the effect of body motions is large in the wave pattern for both cases of λ/B =3.0 and 6.0. In particular, at $\lambda/B = 6.0$, the transmitted wave becomes large and really three dimensional, which is much different from the 2D results.

Finally computed results for the wave drift force are presented in Fig. 5.12 as a comparison between 2D and 3D results. Here the drift force is defined as positive when acting in the direction of incident-wave propagation. The results in Fig. 5.11 are just for a longer body of $L/B = 20$, and we can see favorable agreement between 2D and 3D results except in a limited range of short wavelengths. A discrepancy observed in this range might be attributed to insufficient accuracy in the integration with respect to θ in Eq. (5.70). We can say from Fig. 5.11 that the 2D analysis can be used for estimation of the wave drift force in the design. Although the wave drift force and related mooring force are not considered in computing the wave-induced body motions in the present study, estimation of the wave drift force will be important in actual installation of a floating breakwater.

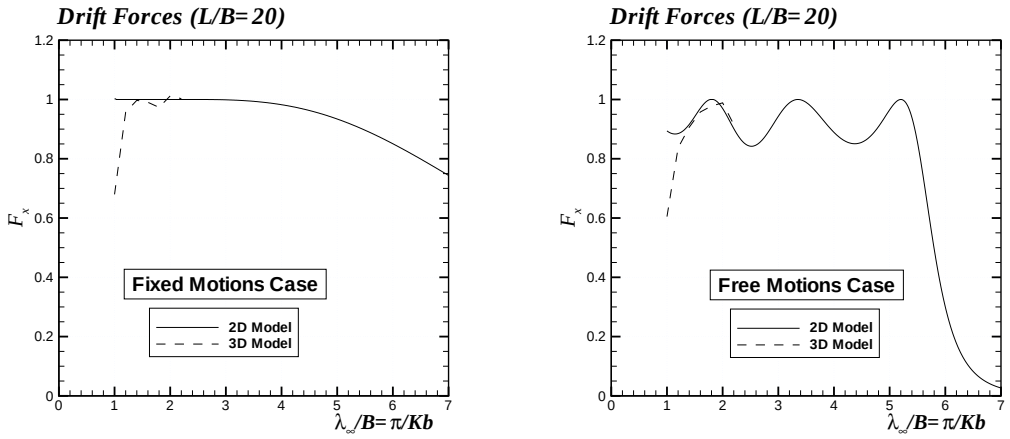

(a) (b)

FIGURE 5.12: Wave drift forces computed by 2D and 3D methods for a body of $L/B = 20$ for both cases of fixed and free motions

Chapter 6

Conclusions

Using genetic algorithm (GA) and boundary element method (BEM) based on the potential-flow theory, a numerical analysis on the performance of floating breakwaters has been performed in both 2D and 3D cases. Some important points found in this study are :

a. A numerical analysis using BEM on floating breakwater with asymmetric shape has been performed. The accuracy and correctness of the analysis were confirmed using several relations and model experiment as well.

b. A scheme based on GA combined with BEM has been exploited to find an optimal model of floating breakwater which has high performance in a wide range of frequencies.

c. By computing for the corresponding 3D model of optimized shape, A difference performance from the 2D model was found. However, the trend in variation with respect to the wavelength becomes similar for longer body which is known as 3D wave effect.

d. 3D wave effects were not so large on the hydrodynamic forces and resultant wave-induced body motions.

e. The free-surface wave elevation was found to be spatially three dimensional even near the middle of a longer body.

f. The drift forces for a longer body were almost the same in values as those for the 2D body.

Bibliographies

[1] F. Mahmuddin and M. Kashiwagi, "Design optimization of a 2D asymmetric floating breakwater by genetic algorithm," *Proceeding of International Society of Offshore and Polar Engineers Conference (ISOPE)*, 2012.

[2] M. Kashiwagi and F. Mahmuddin, "Numerical analysis of a 3D floating breakwater performance," *Proceeding of International Society of Offshore and Polar Engineers Conference (ISOPE)*, 2012.

[3] M. Kashiwagi, "Theory of floating body engineering," *Study Handout*, pp. 1–79, 2006.

[4] M. Kashiwagi, H. Yamada, M. Yasunaga, and T. Tsuji, "Development of a floating body with high performance in wave reflection," *The International Society of Offshore and Polar Engineers (ISOPE)*, vol. 17, no. 1, pp. 641–648, 2006.

[5] F. Mahmuddin and M. Kashiwagi, "Design optimization of a 2D floating breakwater," *Proceeding of the Japan Society of Naval Architects and Ocean Engineers (JASNAOE)*, vol. 12, pp. 515–518, 2011.

[6] D. Coley, *An Introduction to GA for Scientists and Engineers*. World Scientific Publishing, 1998.

[7] S. Sivandam and S. Deepa, *Introduction to Genetic Algorithms*. Springer, 2008.

[8] G. Renner and A. Ekart, "Genetic algorithms in computer aided design," *Computer Aided Design*, pp. 709–726, 2003.

[9] N. Marco and S. Lanteri, "A two-level parallelization strategy for genetic algorithms applied to optimum shape design," *Parallel Computing*, pp. 377–397, 2000.

[10] J. Wehausen and E. Laitone, *Surface Waves, Handbuch der Physik*. Springer-Verlag, Berlin, 1960.

[11] M. Kashiwagi, K. Takagi, N. Yoshida, M. Murai, and Y. Higo, *Hydrodynamics Study of Floating Breakwater*. Seizando Shoten, Co. Ltd, 2003.

[12] T. Haraguchi and S. Ohmatsu, "On an improved solution of the oscillation problem on non-wall sided floating bodies and a new method for eliminating the irregular frequencies," *Trans. of West Japan Society of Naval Architects*, no. 66, pp. 9–23, 1993.

[13] M. Kashiwagi, "A calculation method for steady drift force and moment on multiple bodies (in japanese)," *Bulletin Research Institute for Applied Mechanics, Kyushu University*, no. 170, pp. 83–98, 1995.

[14] H. Maruo, "The drift force on a body floating in waves," *Journal of Ship Research*, vol. 4, no. 3, pp. 1–10, 1960.

[15] J. Newman, "The drift force and momoment on ships in waves," *Journal of Ship Research*, vol. 1, no. 1, pp. 51–60, 1967.